



Key Points:

- We examine the source parameters of the 1949 Khait earthquake, Tajikistan
- We conclude it was predominantly strike-slip on a previously unmapped fault at the Pamir-Tien Shan boundary
- The Khait earthquake shows the hazard posed by “cryptic” faults in the continental interiors

Supporting Information:

Supporting Information may be found in the online version of this article.

Correspondence to:

B. W. W. Johnson,
benedict.johnson@st-annes.ox.ac.uk

Citation:

Johnson, B. W. W., Kulikova, G., Bergman, E. A., Krueger, F., Pierce, I. K., Hollingsworth, J., & Walker, R. T. (2025). Rupture of the 1949 Khait earthquake on a cryptic fault: Implications for earthquake hazard. *Tectonics*, 44, e2024TC008777. <https://doi.org/10.1029/2024TC008777>

Received 17 DEC 2024
Accepted 9 SEP 2025

Author Contributions:

Conceptualization: B. W. W. Johnson, R. T. Walker

Data curation: B. W. W. Johnson, G. Kulikova

Formal analysis: B. W. W. Johnson, G. Kulikova

Funding acquisition: R. T. Walker

Investigation: B. W. W. Johnson, G. Kulikova

Methodology: G. Kulikova, E. A. Bergman, F. Krueger, J. Hollingsworth

Project administration: R. T. Walker

Software: E. A. Bergman, F. Krueger, J. Hollingsworth

Supervision: E. A. Bergman, F. Krueger, I. K. Pierce, J. Hollingsworth, R. T. Walker

Validation: E. A. Bergman, I. K. Pierce, J. Hollingsworth, R. T. Walker

Visualization: B. W. W. Johnson, G. Kulikova

© 2025. The Author(s).

This is an open access article under the terms of the [Creative Commons](#)

[Attribution License](#), which permits use, distribution and reproduction in any medium, provided the original work is properly cited.

Rupture of the 1949 Khait Earthquake on a Cryptic Fault: Implications for Earthquake Hazard

B. W. W. Johnson¹ , G. Kulikova², E. A. Bergman³ , F. Krueger⁴ , I. K. Pierce¹, J. Hollingsworth⁵ , and R. T. Walker¹ 

¹Department of Earth Sciences, University of Oxford, Oxford, UK, ²UP Transfer GmbH at the University of Potsdam, Potsdam, Germany, ³Global Seismological Services, Golden, CO, USA, ⁴Institute for Geosciences, University of Potsdam, Potsdam, Germany, ⁵ISTerre, Université Grenoble Alpes, Grenoble, France

Abstract The 1949 M_w 7.6 Khait earthquake, Tajikistan, was one of the most destructive of the Pamir—Tien Shan region, killing over 7,000 people by building collapse and landsliding. It occurred at the transition between the Pamir and Tien Shan mountain ranges, which converge along the narrow Vakhsh river valley. Therefore, it is important in understanding the tectonic and structural development at the junction of these two major mountain ranges, as well as yielding important information regarding hazard and risk to local populations and infrastructure. Although widespread landsliding and intensities of shaking were recorded, no surface ruptures were mapped, and the earthquake epicenter and source are poorly known. To determine the location, magnitude, and focal mechanism of the 1949 earthquake we combine calibrated earthquake relocations with body-wave amplitude ratios from digitized paper seismograms. Our analysis shows that the earthquake nucleated within the Tien Shan basement with strike slip kinematics. Using high-resolution digital elevation models and orthophotos derived from high-resolution satellite imagery, we identify earthquake ruptures within the epicentral zone consistent with NW-SE right-lateral faulting. Relocated aftershocks and later seismicity also follow a NW-SE trend through the Tien Shan north of the Vakhsh river. Mapping tectonically offset moraines dated in previous literature, we find a Vakhsh Fault slip rate of only half the present day strain accumulation rate derived from GNSS. Our results suggest a significant proportion of the regional deformation may occur away from the geomorphologically well expressed Vakhsh and Darvaz faults, and on faults with little prior expression of activity.

1. Introduction

The 10 July 1949 Khait, Tajikistan earthquake (M_w 7.6) occurred at 09:45 local time (03:53 UTC) and was particularly destructive, leading to over 7,000 deaths predominantly as a result of widespread landsliding (Chen & Molnar, 1977; Evans et al., 2009; Yablokov, 2001). From Kondorskaya and Shebalin (1982): “*in an instant all the buildings in Khait were destroyed...; dust rose from the mountain slides; the entire area became cloudy and instantly grew dark. The ground shook so much that the trees bent to the ground. A car on the road...was tossed and the passengers were flung from the vehicle....*” A shallow earthquake from 1941 of M ~ 6.4 is reported by Kondorskaya and Shebalin (1982) west of Khait (70.5°E, 39.2°N), which caused some damage in the Yasman Valley, but it is unclear if anyone was killed. The 1949 earthquake played an important historical role, triggering the establishment of the Garm Research Station nearby, which became a center of Soviet earthquake research, including into earthquake prediction (Rautian et al., 2007; Sadovsky & Nersesov, 1974).

The Khait earthquake occurred near the Northern margin of the Pamir continental plateau, which is rapidly converging with the Tian Shan to the north at ~13–19 mm/yr: half the north-south India-Eurasia shortening rate at this longitude (Altamimi et al., 2017; Ischuk et al., 2013; Metzger et al., 2020a, 2020b; Zubovich et al., 2010). The faulting accommodating this shortening appears to change along the margin, with relatively simple overthrusting of the Pamir into the Alai Valley, between 72°E and 74°E, contrasting with an increased right-lateral strike-slip component across the Vakhsh river valley of Tajikistan (between 70°E to 72°E). Whether the motion is localized on the geomorphologically well-expressed Vakhsh Fault, or whether strain is accommodated within the basement rocks of adjacent parts of the Pamir and Tian Shan is not resolved.

Despite the high number of earthquakes in the Pamir region, the Khait earthquake is one of only five M_w > 7 instrumentally-recorded earthquakes within the Pamir, of which two are recorded near the Northern Pamir Margin (Figure 1), the other being the 1974 Markansu Earthquake (Jackson et al., 1979). Understanding the source

Writing – original draft:

B. W. W. Johnson, G. Kulikova

Writing – review & editing:

B. W. W. Johnson, G. Kulikova,

E. A. Bergman, I. K. Pierce, R. T. Walker

parameters and causative faulting of the 1949 earthquake thus offers a rare insight into the kinematics and earthquake potential of the Pamir margin. The 1949 earthquake occurred before the establishment of a global standardized seismic network, so the location, magnitude, and focal mechanism are not well resolved. Previous estimates for source parameters and locations are shown in Table 1 and Figure 2. Contemporary scientists were unable to locate surface rupturing from this event but mapped a suite of coseismic landslides including the 4 km-long Khait Landslide, which buried the towns of Khait and Khisorak (Figure 6b) (Gubin, 1960; Leonov, 1960).

To address the existing gaps in knowledge relating to the 1949 earthquake source, we determine an epicenter and focal mechanism from analysis of digitized analog teleseismic records. We use modern regional networks deployed by GFZ Potsdam (Kufner et al., 2018; Schurr et al., 2014) and use multi-event relocation software *mloc* (Bergman et al., 2023) to provide an updated epicenter of the 1949 earthquake, along with a catalog of well-located moderate magnitude earthquakes spanning 1949 to 2017. To map evidence of active faulting and potential earthquake rupturing we acquired 0.3 m resolution Worldview 3, and 0.7 m Pleiades, stereo optical imagery of the northern Yasman Valley and along the major Vakhsh fault, using these to generate 0.5 m Digital Elevation Models (DEMs) and orthophotos. We conclude that the 1949 Earthquake was likely hosted in the Tian Shan basement rock and is unlikely to have activated the major Vakhsh Fault. This shows that while simple overthrusting occurs in the Alai Valley, in the Vakhsh Valley, where the previous sedimentary basin has completely closed, the zone of deformation has expanded to include the Tian Shan basement.

2. Seismotectonic Setting

The Pamir Mountains form an extensive high-altitude continental plateau within the ongoing India-Eurasia collision, west of the larger Tibetan plateau (Burtman, 1993). They are bounded to the east by the low-lying and relatively undeformed Tarim basin (Neil & Houseman, 1997); to the north by a series of narrow and partially consumed sedimentary basins that separate the Pamir from the Tien Shan mountain ranges (Leith & Alvarez, 1985; Sobel et al., 2013); and to the northwest and west by the Afghan-Tajik depression, which is a large sedimentary basin that is deforming internally (Gagała et al., 2020; Kufner et al., 2018; Sobel et al., 2013) (Figure 1).

The Pamir are composed of accreted terranes from the Paleozoic to Cenozoic with arcuate sutures. Terrane sutures are offset northward within the Pamir relative to Tibet and the Hindu Kush by 300–700 km indicating the Pamir have moved northward toward Eurasia relative to the Tibetan Plateau and Hindu Kush during Cenozoic times (Burtman, 1993; Schwab et al., 2004).

The Pamir Frontal Thrust (PFT) and Main Pamir Thrust (MPT) accommodate around 10 mm/yr north-south convergence (Arrowsmith & Strecker, 1999; Coutand et al., 2002; Patyniak et al., 2021; Zubovich et al., 2016). Westward, the north-south compression is taken up by the Vakhsh Thrust System and Darvaz Fault (Figures 1 and 2). Subduction beneath the southern and northern margins of the Pamir to depths of ~300–350 km is indicated by earthquake locations (Sippl, Schurr, Tympel, et al., 2013) seismic tomography (Kufner et al., 2016; Sippl, Schurr, Yuan, et al., 2013), receiver functions (Schneider et al., 2013, 2019), guided wave observations (Mechie et al., 2019). The Alai Valley is thought to be subducting beneath the Pamir, but along strike near Khait, subduction has terminated.

The Vakhsh Thrust is the leading thrust of the Peter I Range: a fold and thrust belt formed by compression of Tajik Basin sediments between the Tian Shan and Pamir (Gagala et al., 2020; Leith & Alvarez, 1985). Thrust earthquake focal mechanisms strike parallel to the surface trace of the Vakhsh fault (Hamburger et al., 1993; Kufner et al., 2018; Schurr et al., 2014). The fault is exposed as a plane of evaporite, with quaternary scarps, near to the Obikhingou river (70.1114°E, 38.8536°N) (Gagala et al., 2020). GNSS velocity profiles perpendicular to the Vakhsh valley near Garm show both 17 mm/yr shortening and 13 mm/yr right-lateral shear, and it has been suggested that the Vakhsh fault accommodates the strike-slip motion aseismically while accommodating the thrusting seismically (Metzger et al., 2020a, 2020b). Closer to Khait, however, the shortening across the Vakhsh Fault appears to be ~5 mm/yr. Aseismic creep has been observed along the westward continuation of the Vakhsh fault (Metzger et al., 2021). It is currently unknown whether the Vakhsh Thrust has hosted a large historical earthquake.

Near Khait, PT axes from earthquake focal mechanisms indicate WNW-ESE compression (Kufner et al., 2018; Lukk et al., 1995; Schurr et al., 2014) (Figure 2b). This deformation is thought to be concentrated onto the Vakhsh

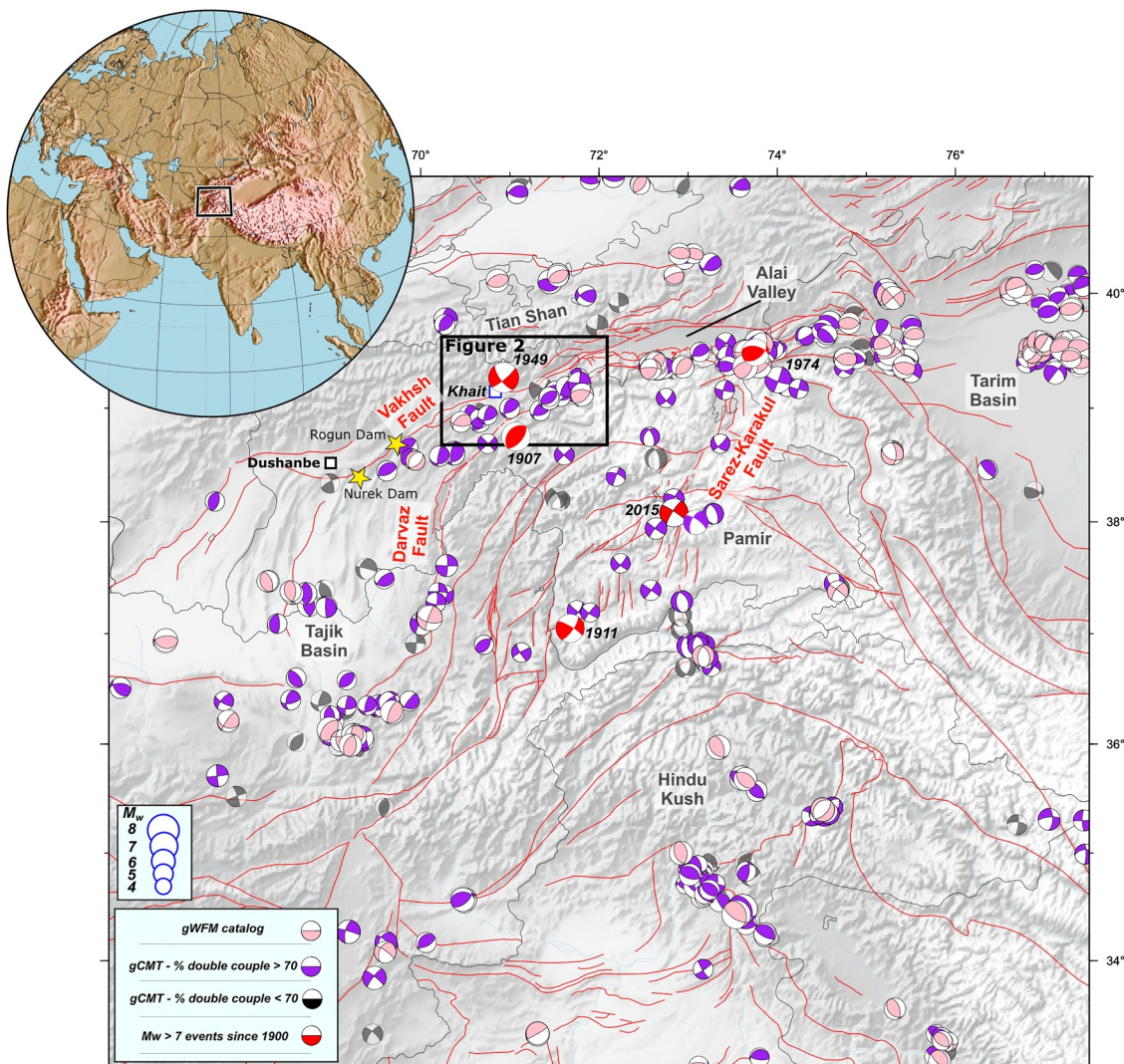


Figure 1. Earthquake mechanisms of the Pamir and surroundings from the gWFM (Wimpenny & Watson, 2020), and gCMT (Dziewonski et al., 1981; Ekström et al., 2012) catalogs, with locations from the ISC-EHB catalog where available (Engdahl et al., 1998, 2020; Weston et al., 2018). gCMT mechanisms are split into those above and below 70% double couple. Earthquakes of $M_w > 7$ since 1900 are shown in red, with mechanisms and locations from Elliott et al. (2020), Jackson et al. (1979), Kulikova (2016), Mikhailova et al. (2015). Faults are from the Central Asia Fault Database (Mohadjer et al., 2016). Mechanisms along the Northern Pamir Margin and show shortening in this region. This is consistent with GNSS studies which show 13–19 mm/yr convergence between the Pamir and Tian Shan. In the Pamir interior, crustal earthquakes are focused along the strike-slip Sarez-Karakul Fault Zone and in a normal earthquake zone in the southern Pamir. These accommodate east-west extension across the Pamir Plateau observed in the GNSS. This east-west extension is accommodated in the Tajik Basin by folding along north-south axes. The strike slip Darvaz Fault is picked out by left lateral strike slip mechanisms, but the right lateral Vakhsh Fault appears to be a mixture of right-lateral strike-slip and thrusting. Along the Northern Pamir Margin, the Pamir overthrust the Alai Valley along the Pamir Frontal Thrust. Near Khait, this shortening is accommodated across several faults, including the Vakhsh Fault.

and Darvaz Faults (Hamburger et al., 1993; Metzger et al., 2020a, 2020b; Schurr et al., 2014; Trifonov, 1978). However, earthquake location uncertainty and the prevalence of landslides and mass movement scarps make it difficult to positively identify earthquake surface ruptures and fault scarps (Strom & Abkhmatov, 2018). Where fault scarps are present, they are discontinuous along strike.

The Darvaz fault runs down the western side of the Pamir, with earthquake focal mechanisms indicating it to be a vertically dipping left-lateral strike-slip fault (Kufner et al., 2018; Lukk et al., 1995; Schurr et al., 2014). GNSS profiles perpendicular to the fault in the western Pamir show 10–15 mm/yr left lateral shear with ~10 mm/yr extension. Soviet-era paleoseismic studies of the Darvaz Fault near Saghirdasht (70.66°E , 38.64°N) suggested strike-slip rates of 12–14 mm/yr, but their dating is uncertain (Trifonov, 1978). It is suggested the Darvaz fault

Table 1*Previous Estimates of 1949 Khait Earthquake Source Parameters*

Longitude/deg	Latitude/deg	Depth/km	Strike/deg	Dip/deg	Rake/deg	Magnitude	Reference
70.8706	39.3364	22 ± 5	50 ± 20	80 ± 10	-20 ± 10	MS 7.8/m _B 7.6/M _w 7.6	This Study
70.8915	39.1739	20 (fixed)	-	-	-	MS 7.3	ISC—Storchak et al. (2017)
70.8	39.2	16	-	-	-	MLH 7.4	Kondorskaya and Shebalin (1982)
-	-	-	-	-	-	M _w 7.5	Chen and Molnar (1977)
-	-	-	-	-	-	M _w 7.5	Chen and Molnar (1977)

continues to the northern margin of the Pamir and links up with the Main Pamir Thrust (MPT) (Schurr et al., 2014; Sobel et al., 2013) although this is difficult to follow in the landscape. Our own mapping and earthquake locations suggests a more complicated junction between these faults where N-S shear zones act to accommodate differential longitudinal convergence rates (Section 4.1, Figure 10).

The northern Pamir margin has very high relief and is glaciated. Lying at the convergence between the Indian Summer Monsoon and the Mid-Latitude Westerlies, Pamir glaciation is modulated through time by the relative strength of these weather systems (Benn & Owen, 1998). This leads to incomplete and asynchronous preservation of glacial stages within the Pamir (Dortch et al., 2013). There is evidence of glacial advances in the Pamir at 16–12 ka, 24–28 ka, ~65–40 ka, ~80–60 ka, ~200–100 ka, and >200 ka (Abramowski et al., 2006; Röhringer et al., 2012; Seong et al., 2009; Stübner et al., 2017, 2021; Wang et al., 2011; Zech et al., 2005).

Closer to Khait, the Fedchenko Glacier is the largest in the region, lying at the north-western edge of the Pamir. It feeds into the Muksu Valley which joins the Vakhsh near Sary Tala (Figure 7). This has deposited lateral and recessional moraines in the Vakhsh Valley at ~18 kyr which are tectonically offset (Grin et al., 2016) (Figure 7). South of Sary Tala, in the Peter I Range, there is a small complex of moraines within a region ~10 km × 8 km showing evidence of up to nine advances, which are also cut by a tectonic scarp (Figures 2c and 8). We suspect these smaller moraines postdate 18 ka, because they are not as extensive as we might expect and there is evidence for at least one Little Ice Age advance in the nearby Abramov Glacier over the past thousand years (Saks et al., 2024).

This glacial history has produced steep sided valleys throughout the region prone to landsliding and has concentrated human activity into comparatively little space on terraces. These factors present challenges in finding and assessing evidence of active faulting in the geomorphology, but also allow some age constraint on the tectonic geomorphology.

For these reasons, geomorphic evidence for the 1949 Khait Earthquake has so far been limited to damage and landsliding. These were mapped in the decades following the earthquake (Gubin, 1960; Leonov, 1960) (Figure 2a). When contoured, these data show a WSW-ENE elongation, consistent with both a shallow (i.e., crustal) earthquake source and a fault striking sub-parallel with the Vakhsh Fault. Coseismic landslides are concentrated north of the Vakhsh river valley, concurring with damage to settlements in the region (Figure 2a). In the remote mountainous regions north-east of Khait mapping and damage data are lacking, so the intensity contours are unconstrained. Taken together, the available macroseismic evidence suggests the 1949 earthquake ruptured a fault north of the Vakhsh Fault. The maximum intensity close to Khait was 10 on the MSK scale representing “general destruction of buildings” (Medvedev et al., 1965). Dushanbe, ~200 km away, suffered “light damage to brick buildings” and cities as far away as Samarkand, ~350 km, felt enough shaking to “awaken people.”

3. Materials and Methods

3.1. 1949 Source Parameters Determination Using Analog Seismic Data

The 1949 Khait earthquake was recorded by many seismic stations worldwide providing a wide azimuthal coverage (Figure 3a) for seismic data. The old seismic bulletins (e.g., Storchak et al., 2015) offer arrival times for various phases, which significantly contributes to the data required for determining epicenter location. However, many of the original analog seismic records (the original paper seismograms) have not been available to us.

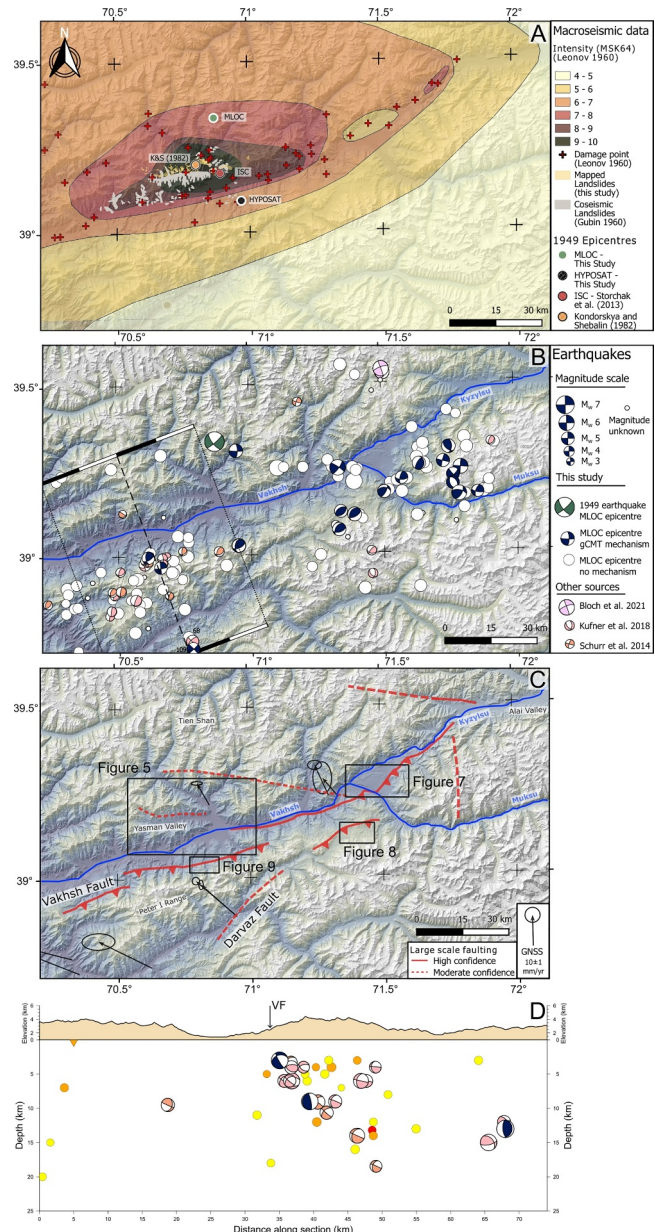


Figure 2. (a) Isoseismals from the earthquake based on data (red crosses) from Gubin (1960) and Leonov (1960) using the MSK64 scale (Medvedev et al., 1965). Previous location estimates for the 1949 earthquake epicenter are shown along with the location from this study (labeled *mloc*). The elliptical damage contours are consistent with a crustal depth earthquake, and the long axis is roughly parallel to the Vakhsh Valley suggesting a source roughly parallel to this valley. The contour shapes may be biased by the lack of data to the north-east of Khait, and by the landslide susceptibility of the Yasman Valley, further discussed in the text. (b) Earthquake focal mechanisms and epicenters relocated using *mloc*. Our relocation puts the 1949 M_w 7.6 Khait Earthquake (dark green) ~30 km north of the Vakhsh Valley and waveform modeled mechanism indicates right lateral strike-slip on a N-W or S-W-striking fault. The Vakhsh Fault is defined by a cluster of right-lateral strike-slip/thrust mechanisms in a diffuse alignment with the Valley. In cross section (d) (section line and width in panel b) these thrusts lie on a ~50° dip angle, roughly parallel to the mechanism focal planes. We do not observe earthquakes at around (71.2°E, 39.0°N). Around where the Darvaz and Vakhsh Faults would be projected to intersect. (c) Solid red lines show high confidence fault mapping based on long term geomorphic offsets, and dashed lines show lower confidence mapping based on earthquake mechanism alignments. GNSS vectors from Metzger et al. (2020a, 2020b) show both right-lateral motion along the Vakhsh valley, and contraction across it. The station spacing is such that this motion cannot be allocated onto discrete faults.

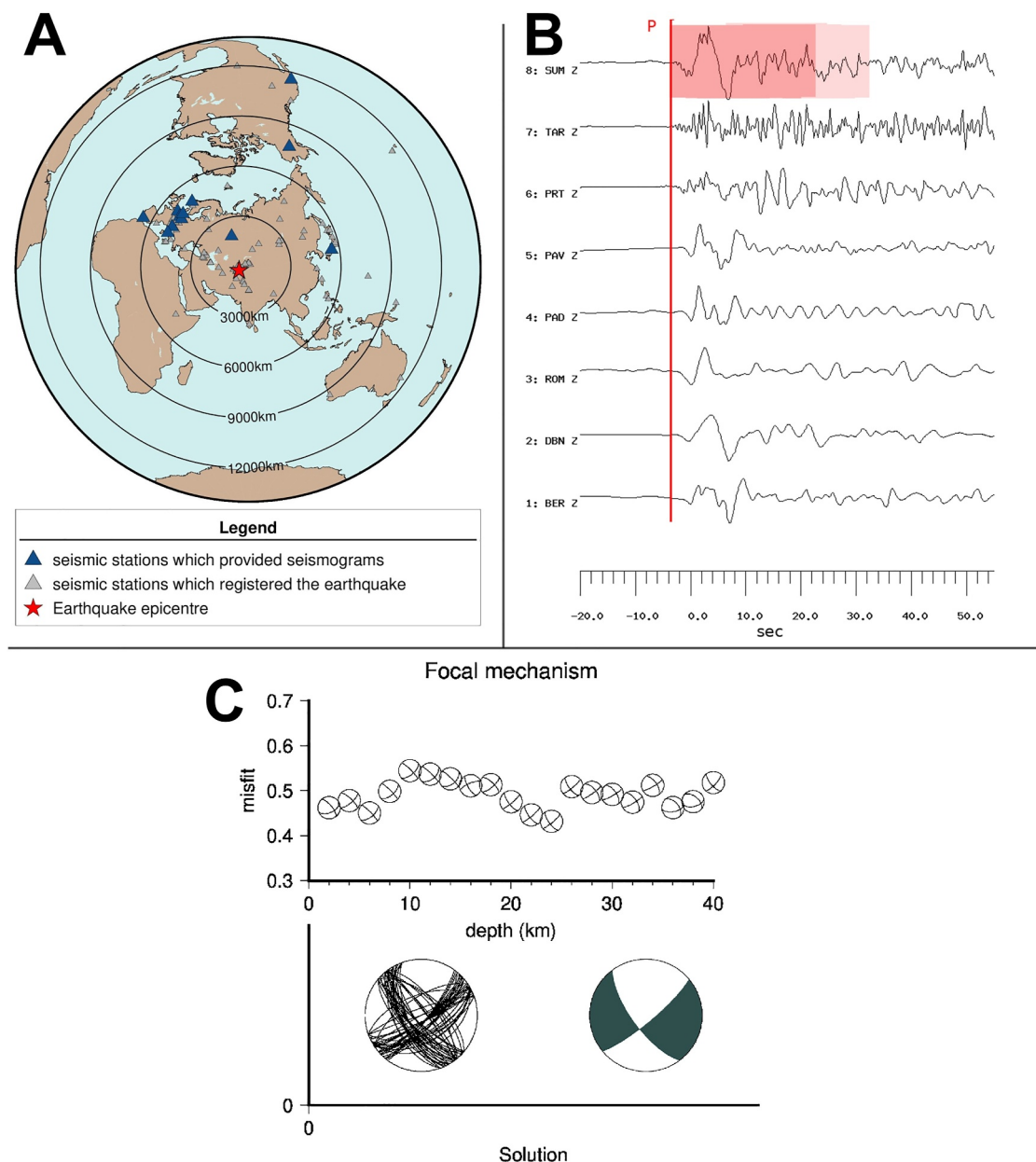


Figure 3. (a) Azimuthal distribution of all (according to the information provided in seismic bulletins) seismic stations (gray triangles), which recorded the 1949 Khait earthquake (red star); dark blue triangles show seismic stations whose records were digitized for focal mechanism determination. (b) Digitized Z components from European stations show a mixture of strong and weak P wave arrivals, consistent with Europe's location near the nodal plane of the focal sphere. The upper trace shows normalized to the maximum sum of all the traces (SUM). The apparent source time duration estimated from apparent P wave duration by visual inspection lies between 25 (colored dark red) and 35 (colored light red) seconds which suggests a similar rupture duration. (c) (Upper plot) The dynamics of the misfit function concerning the earthquake's depth shows a minimum occurring at depths ranging from 22 to 24 km. The top 5% of solutions, represented by the dark green beach ball, illustrates the focal mechanism that exhibits the lowest misfit.

Altogether we have collected the records from 42 seismic stations (gray triangles Figure 3a). But only records from 12 stations were suitable for digitization due to the poor quality of the scanned paper records.

The nearest stations, within the former USSR located closer than 3,000 km to the epicenter had to be excluded for waveform modeling as their amplitudes exceeded the amplitude range of the seismometer, clipping the data. The remaining stations were mainly located in Europe, with three in Japan and the United States. Among the 12 stations used, eight were situated in Europe, with seven of them being in close proximity to each other. Therefore, the seismic network in Europe served as a large aperture seismic array. This allows the alignment and stacking of

records, thereby enabling the identification of coherent wavelets generated by the source. For P-waves, this process is relatively straightforward (see Figure 3b), allowing us to generate a summation trace (SUM Z, Figure 3b) which tells us the rupture duration. We use this in Section 5.1 to estimate the length of the 1949 rupture. While the azimuthal coverage is not ideal, and greater coverage would reduce source parameter uncertainties (Table 1), we have stations that sample at least two quadrants of the focal sphere. In addition, one focal plane should pass through Europe and the other focal plane should pass between the Japanese and American stations, providing additional constraints, although having one nodal plane constrained by two stations is not ideal.

The majority of available analog seismograms were recorded by the instruments consisted of mechanical pendula hinged to a stylus writing onto a slowly rotating drum. Minute marks tracked time on the records, and different stations were synchronized to a universal clock. The paper records were scanned at high resolution, and manually digitized using vector graphics software (we have used GIMP, (The GIMP Development Team, 2025)). The lines were smoothed with Bezier Curves, resampled at a 0.1 s interval and converted to ASCII text format. Curvature of the trace due to the cylindrical drum was corrected using the method of Cadek (1987) and Grabovec and Allegretti (1994).

We derived a preliminary epicenter location for the 1949 using HYPOSAT (Schweitzer, 2001, 2018). This software can use absolute arrivals as well as arrival times (e.g., S-P) differences. By using both, we determined the epicenter location and origin time of the earthquake. We observed timing errors on the order of up to 5 s between different stations, which may be attributed to uncertainties in phase picking, errors in minute marks on the digitized seismograms, or time misalignment across various stations. This resulted in a considerable location error ellipse of up to 20 km in latitude and 40 km in longitude. Consequently, the calibrated earthquake relocations (Section 3.2) was necessary.

A number of issues preclude using routine moment tensor inversion techniques (Dahm & Krüger, 1999, 2014) for focal mechanism and seismic moment determination of the earthquake in our case. Firstly, the bandwidth of the analog seismic instruments at that time was not always sufficient to record the lower frequencies of large earthquakes ($M_w > 7$). Teleseismic moment tensor inversion is often performed using 15–100 s bandwidths (Talebian & Jackson, 2004) but instruments in 1949 had bandwidth between 4 and 10 s (Wiechert inverted pendulum), sometimes going up to maximum 20 s (Bosch-Omori instruments) (McComb & West, 1931; Wood, 1921). Secondly, frequency artifacts caused by the writing needles dislocating during strong shaking, and steps introduced when interpolating the trace across paper records affected the moment tensor solution. Thirdly, different components of motion could be misaligned in time or absent. For example, we were able to acquire only the Z component for station BER, and only the E-W component for station DBN. This is problematic, as moment tensor inversion often requires recordings from all perfectly aligned in time three components (NS, EW, and Z) in order to derive radial and transverse components of motion. Finally, instrument calibration information was not always available or certain for every station and sometimes needed to be extracted from the literature (Wood, 1921; Appendix D) where only reference values are given—not those for a specific day and time. This information is necessary to deconvolve the instrument response from the trace and extract the actual displacement (Scherbaum, 2006).

Given the problems in using conventional moment tensor inversion to determine the focal mechanism, we instead used a comparison of amplitude ratios between observed and synthetic seismograms in order to determine the focal mechanism. Synthetic waveforms were produced using synthetic Greens function database calculated with the FOMOSTO tool in the PYROCKO (Heimann et al., 2017, 2019) framework. In a grid search the synthetic records were simulated for different strike, dip and rake and their amplitude ratios (for P, PP, S, SS phases) were compared to corresponding amplitude ratios of the observed seismograms and misfit was calculated. These calculations were repeated for different test depths using a depth increment of 2 km. The minimum misfit between observed and modeled amplitude ratios determines the strike, dip and rake angle (focal mechanism, Figure 3c Bottom) and the most probable depth (Figure 3c Top) of the earthquake. For a more detailed account of this method see (Kulikova & Krüger, 2015; Ou et al., 2020). It is frequently observed that paper records lacked distinct polarity indicators; consequently, the first motion polarity on the Z-component, which serves as a definitive marker for the compressional and dilatational quadrants, could not be ascertained. In such instances, we must depend on alternative data, such as geological observations, to accurately identify the true fault plane. Regarding the 1949 Khait earthquake, there was one station (ROM, Italy) that provided a clear indication of the polarity,

which was subsequently used. The focal mechanism is constrained to be a double-couple, although our geomorphic analysis indicates the source was probably more complex (Section 5.1).

For the 1949 Khait earthquake, we computed three distinct types of magnitude: m_B , M_S and M_w . The broadband body wave magnitude m_B (Bormann & Saul, 2009; Bormann et al., 2013; Appendix A) and the surface wave magnitude M_S (using the Prague-Moscow Formula (Karnik et al., 1962)) were derived from the amplitude and period values obtained from the digitized waveforms (see Appendix B). While the measurement of amplitude and period for body waves is relatively straightforward and yields reliable values, the amplitude measurement for surface waves presents complexities. The Prague-Moscow Formula (Karnik et al., 1962) for M_S necessitates measurements at longer periods, approximately 20 s. However, this poses challenges for analog instruments, as previously noted, since most instruments of that era had bandwidths ranging from 4 to 10 s. Consequently, the recorded surface wave signals experience amplitude saturation and insufficient amplitude measurement at lower frequencies. M_w was calculated by fixing the focal mechanism (as determined with amplitude ratios comparison) and generating synthetic seismograms at different magnitudes to find the closest match to the observed amplitude (Appendix C). For a more detailed account of this method see (Kulikova & Krüger, 2015; Ou et al., 2020).

3.2. Calibrated Earthquake Relocations

3.2.1. Overview

There is significant uncertainty and variance in reported epicentral location of the 1949 earthquake (Kondorskaya & Shebalin, 1982; Storchak et al., 2015). The preliminary location determined using HYPOSAT in the previous section still has a 40 km uncertainty, and this is not sufficient to assign the earthquake to a fault in this region, and so elucidate the tectonic role of this earthquake.

Previously reported estimates of epicentral location were based on macroseismic evidence (Kondorskaya & Shebalin, 1982; Storchak et al., 2015). These are sited close to Khait town, though this may be due to a lack of regionally extensive data. Damage report coverage (Figure 2a, red crosses) is unevenly distributed, with a particular gap to the north-east of Khait, so the exact shape of the damage contours is uncertain, and additionally the damage data do not always distinguish between damage caused by shaking and landsliding. Kondorskaya and Shebalin (1982) report that “*The village of Khait and 20 kishlaks [settlements] were buried by the slides in the Yasman River valley.*” Evans et al. (2009) have argued that sediments in the Yasman Valley would have had a particularly high susceptibility to shaking-induced landsliding, being composed of loess and saturated from rain during the night of 9–10 July 1949 (Stanyukovich, 1997). Therefore, there is reason to believe the very high amounts of landsliding may not correlate well with the region of greatest ground motion, so do not help us pinpoint the earthquake epicenter.

Previous seismotectonic studies are unclear whether the Khait earthquake nucleated and was hosted on the large-scale Vakhsh Fault or on faults in the Tian Shan (Hamburger et al., 1993; Schurr et al., 2014). We were unable to find extensive surface ruptures on the southern side of the Vakhsh Valley, and recent GNSS and satellite radar measurements further west imply the Vakhsh Fault may be creeping (Metzger et al., 2020a, 2020b, 2021), possibly due to evaporites within the fault, as observed in surface outcrops of the fault plane near the Obikhingo river (Gagala et al., 2020).

We refine the location of the 1949 earthquake by including it in a calibrated cluster of earthquakes analyzed with the program *mloc* (Bergman et al., 2023). *mloc* is based on the hypocentroidal decomposition (HDC) algorithm introduced by Jordan and Sverdrup (1981) but it incorporates additional procedures to produce (if appropriate data are available) hypocenters that are minimally biased by unknown Earth structure and that have realistic parameter uncertainties based on the variability of the data used. Relocations with these properties are referred to as “calibrated.” The use of *mloc* in this study exactly parallels the relocation studies contributing to the Global Catalog of Calibrated Earthquake Locations (GCCEL), as described in Bergman et al. (2023).

Like all multiple event relocation algorithms *mloc* uses differences in observed arrival times of seismic phases to improve the relative locations of a set of earthquakes within a limited area (termed a “cluster”). Uniquely among such algorithms, however, the hypocentroidal decomposition method uses projection operators to split the relocation problem into two parts. At each iteration, improvements to the relative locations, or “cluster vectors,” of the events in the cluster (relative to a reference point called the hypocentroid) are determined. Next, improvements to the absolute location of the hypocentroid are determined in close analogy to a single event location,

but using data selected from all the events in the cluster. After each iteration the cluster vectors are added to the hypocentroid to obtain absolute locations for the individual events. The choice of data used for the hypocentroid determines whether a converged relocation can be considered calibrated or not. For example, to relocate clusters in oceanic or remote continental areas lacking nearby seismograph stations, the hypocentroid might be located with teleseismic P arrivals. Such a cluster would not be considered calibrated, as the arrival time data would be biased by unknown Earth structure.

For this study, the hypocentroid was determined from direct-arriving local phases (Pg and Sg) within 1.0° of each event in the cluster. Since the relative locations (cluster vectors) of all events have been determined in the first step of the relocation, these arrival times can be utilized to locate the hypocentroid as if it were an earthquake. Since the ray paths of the arrival time data used to establish the absolute location of the cluster (i.e., all the included events) are short, the biasing influence of unknown Earth structure is minimized. There is an obvious tradeoff between the limiting distance for data used to estimate the hypocentroid and the number of data used (and thus statistical power). The epicentral distance limit used here, 1.0° , is very typical for the calibrated clusters in GCCEL. To the extent that this distance range still encompasses significant lateral heterogeneity, the scatter introduced in the arrival time data will be reflected in the so-called empirical reading errors used for inverse weighting, and the parameter uncertainties will reflect that heterogeneity. Figure 4 illustrates this application of *mloc*.

The relocation process is iterative, both in a single run of *mloc*, but also in the sense that many runs are needed to properly deal with outlier readings and other sources of bias.

3.2.2. Treatment of Errors

Multiple event relocation allows for error treatment using the statistics of the arrival time data, which is not possible for single-event relocation. Errors in reported phase arrival times arise from multiple sources, including varying signal-to-noise levels, variations in analyst (or automatic) picking strategies, interference from multiple phases arriving close together, timing errors and differences in the precision to which arrival times are reported. At each run *mloc* produces an output file of the spread and mean of arrival times for each distinct station-phase pair (“empirical reading error”), using a robust estimator of spread. After the first run the empirical reading errors from the previous run are used for inverse weighting of the arrival time data. Empirical reading errors have a minimum value of 0.1 s so they cannot become unrealistically low.

It is essential to use a robust estimator of spread, meaning one that is insensitive to gross outliers, in this process so that outlier readings are exposed. *mloc* employs the “Sn” algorithm (Croux & Rousseeuw, 1992). Outlier readings are flagged in the event data files by the user between runs, either manually or with a utility program. This needs to be done gradually, taking only the greatest outliers each time, until the set of residuals for each station-phase approximates a normal distribution when normalized by the empirical reading error and mean residual (Figures 4b and 4c; Figure S7 in Supporting Information S1). The mean residual is interpreted as the correction for whatever velocity model has been used to calculate the theoretical travel time for that station-phase, but this information is not relevant in *mloc*, except for the local-distance readings used for the hypocentroid, because all other arrival time data are utilized only as differenced travel times.

For the 1949 earthquake timing synchronization errors to a world clock may have been an issue for some stations. We don't have a good idea of the magnitude of this uncertainty, but the HYPOSAT single event location analysis indicates that all residuals between observed and modeled travel times are of the order of 5 s (Section 3.1). This suggests the timing errors arising from synchronization problems are less than this. Assuming synchronization errors between different stations that recorded the 1949 earthquake are independent, these would contribute to a larger location uncertainty, and not a systematic bias in the location. Therefore *mloc* likely deals with these synchronization errors as well as any other random error described above.

3.2.3. Depth Control and Velocity Model

We use the ak135 global 1-D velocity model (Kennett et al., 1995) with a modified crust such that the travel time residuals in the distance range used for the hypocentroid are minimized (see Appendix E). The crustal velocity model and event depths were refined during the initial runs with a set of events having especially good local data,

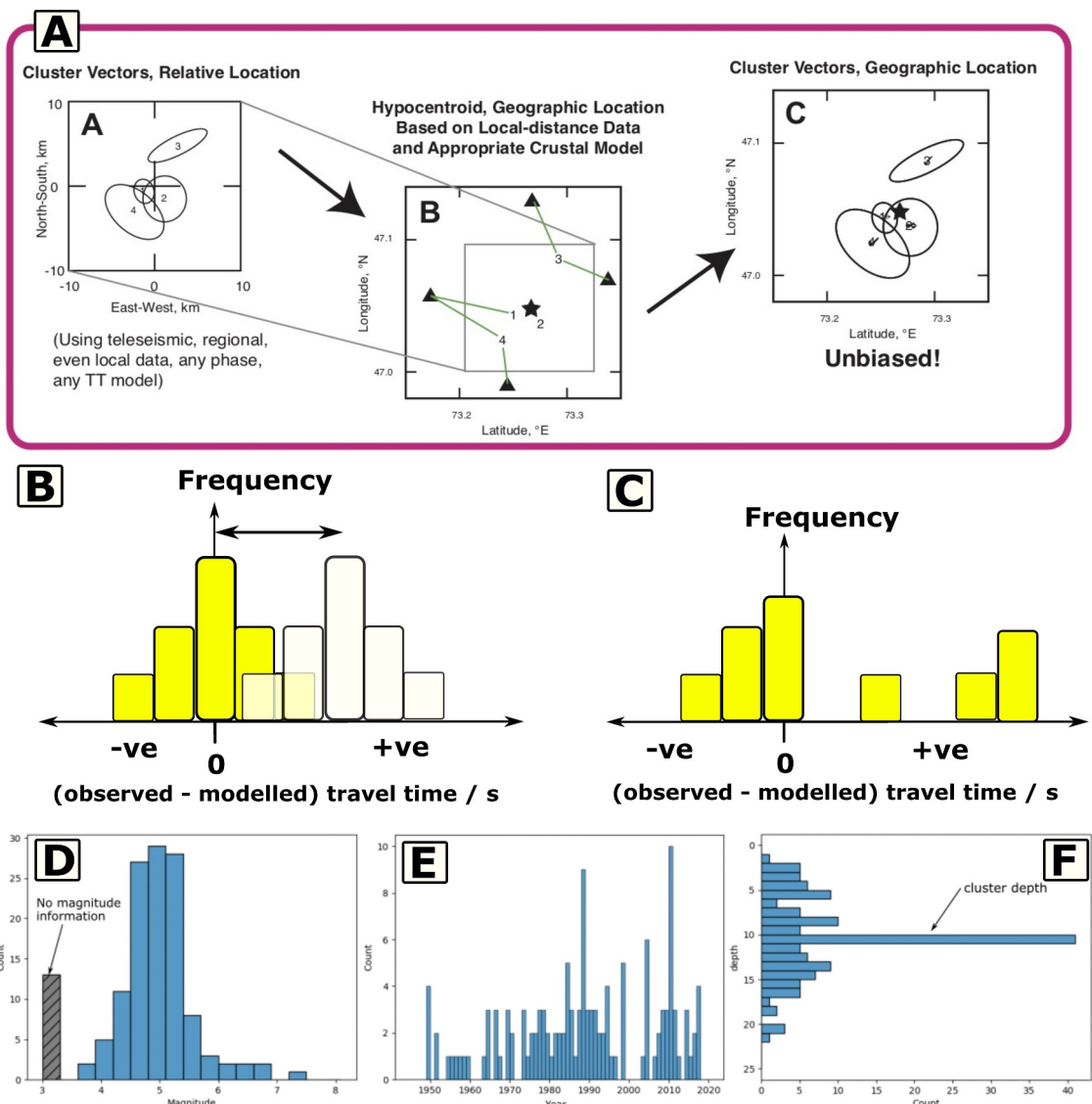


Figure 4. (a) Flowchart for the Hypocentroidal Decomposition Algorithm that *mloc* uses to determine calibrated locations. Calibration events are those with regional station data from the TIPAGE (2008–2012) seismometer deployment (Schurr et al., 2014). The calibration is then used to determine an unbiased location for the 1949 Khait Earthquake, despite there being limited contemporaneous seismometer coverage. (b and c) Sketch histograms of P phase arrivals for a station where many earthquakes in the cluster were recorded. (b) Shows the case where there is a random error introduced by picking mistakes, and a systematic error introduced by a combination of picking strategies, consistent misidentification of a phase, and station timing error. These errors are automatically dealt with by the algorithm. In (c) we see the case where there is a systematic error affecting the phase arrivals, but it only affects some of the data. This is not dealt with by the algorithm and requires manual data cleaning using tools in *mloc*. (d, e, f) Histograms of magnitude (d), year (e), and depth (f) for earthquakes within the cluster. The bar in (f) labelled “cluster depth” shows events with no depth constraint which were arbitrarily fixed to 10 km.

with near-source arrivals (less than about 1.5–2.0 focal depths) to constrain focal depth. Once the crustal part of the model is established the crustal thickness is adjusted to fit the observed Pn arrivals.

Once the velocity model is set, the depths of other events lacking near-source arrivals can often be usefully estimated. If events only have one or two direct arrival times $\sim 1^\circ$ epicentral distance, and their depth can't be found using direct arrivals alone, another approach for depth constraint can be used. The “Local Distance Method” exploits the dominance of Pn arrivals in most event data sets. With epicenters stabilized by the abundance of data at all distances and azimuths, the Pn data tend to dominate the estimate of origin time, for a given assumed depth. If there are any direct crustal arrivals in the range beyond near-source but closer than the Pg/Pn crossover distance, their travel times are mainly influenced by the origin time, not focal depth, since for shallow

events the raypath is nearly horizontal. Therefore shifting the focal depth causes changes in the residuals of those far-local arrivals in the same sense (but less precision) as for near-source arrivals, and thus gives a way to estimate focal depth. Focal depths determined in this way are vulnerable to the arrival time errors for the direct arrivals, as usually there are only one or two of these (Karasözen et al., 2016, 2019).

Depths can also be usefully estimated from teleseismic depth phases, various types of waveform modeling and fault models derived from InSAR data.

3.2.4. Event Selection

The cluster for this study includes 133 earthquakes that were large enough to have arrival time data at teleseismic distances from the ISC Bulletin (Storchak et al., 2017, 2020) (Table 1). Other arrival time data came from the TIPAGE and TIPTIMON earthquake catalogs (Kufner et al., 2018; Schurr et al., 2014) and the historical seismogram digitization described in Section 3.1. Arrival time data for early aftershocks of the 1949 event was hand digitized from the ISS bulletin (Villaseñor & Engdahl, 2005).

We prioritized an even time distribution of events in order to strongly link the locally-recorded events of 2008–2010 to the 1949 earthquake (Figure 5b). We chose events on the basis of having >100 phase arrivals rather than magnitude, as some of the pre-1960 events lacked magnitude information. This cluster included all events with a gCMT focal mechanism (Dziewonski et al., 1981; Ekström et al., 2012) and provided a magnitude range of M_w 3.8–6.9 (Figure 5a). We also prioritized events close to a regional seismometer as this gave us better depth control (see Section 3.2.3). Where no depth control was possible, we assigned a default cluster depth of 10 km (Figure 5c). This does not affect the epicentral estimate when there is good azimuthal coverage, as any bias in depth is compensated in the origin time (Shearer, 2019, p. 127).

3.2.5. Relocation Strategy

Because of the large changes in the constellation of observing stations across this cluster, we adopted a gradualist strategy for the relocation, beginning with a set of seven events, ranging in magnitude from 3.7 to 5.1, that were closely observed by the TIPAGE deployment between October 2009 and May 2010; they were also recorded by regional and teleseismic stations. In the process of relocating these events, which have good depth control from near-source stations, the crustal velocity model was also refined.

Starting from this kernel of well-located events, the cluster was gradually expanded by adding the events nearby in time. At each increment in building the cluster, several runs are used to refine the hypocentral parameters and arrival time data sets, flagging outliers and estimating empirical reading errors.

The final calibrated hypocenters of the cluster are listed in Table 2.

3.3. Geomorphic Analysis

We acquired high-resolution stereo optical satellite imagery and constructed digital elevation models (DEMs) of the Vashkh fault and the 1949 epicentral region, in order to identify evidence of recent fault slip, to measure scarp heights, slip vectors, and to map out geomorphic units displaced by faulting. We used 0.3 m Worldview 3 stereo and 0.5 m Pleiades stereo imagery. Point clouds for the satellite DEMs are available for download on OpenTopography (add DOI).

The DEM construction approach uses the disparity between satellite images taken from different positions of the same point, disparity being the vector required to map a pixel from one image onto the equivalent pixel in the other image. Position, orientation and camera model are read from the Rational Polynomial Coefficients (RPCs) supplied with the imagery. Once the RPC model is accounted for, the remaining disparity in the images is assumed to be stereoscopic distortion from topography and can be used to construct a 3D point cloud. This can be gridded based on the average point height inside a cell to produce a DEM. The hillshaded DEM is then used for mapping and profiling possible fault scarps. The Pleiades imagery was processed using Agisoft Metashape Professional version 1.6 (<https://www.agisoft.com/downloads/installer/>). The Worldview 3 was processed with the NASA Ames Stereo Pipeline version 2.6.2 (Beyer et al., 2018, 2021; Shean et al., 2016). Gridding at a higher resolution allows us to resolve small scale features in the point cloud, but also increases the noise in the DEM, so care is required when interpreting features.

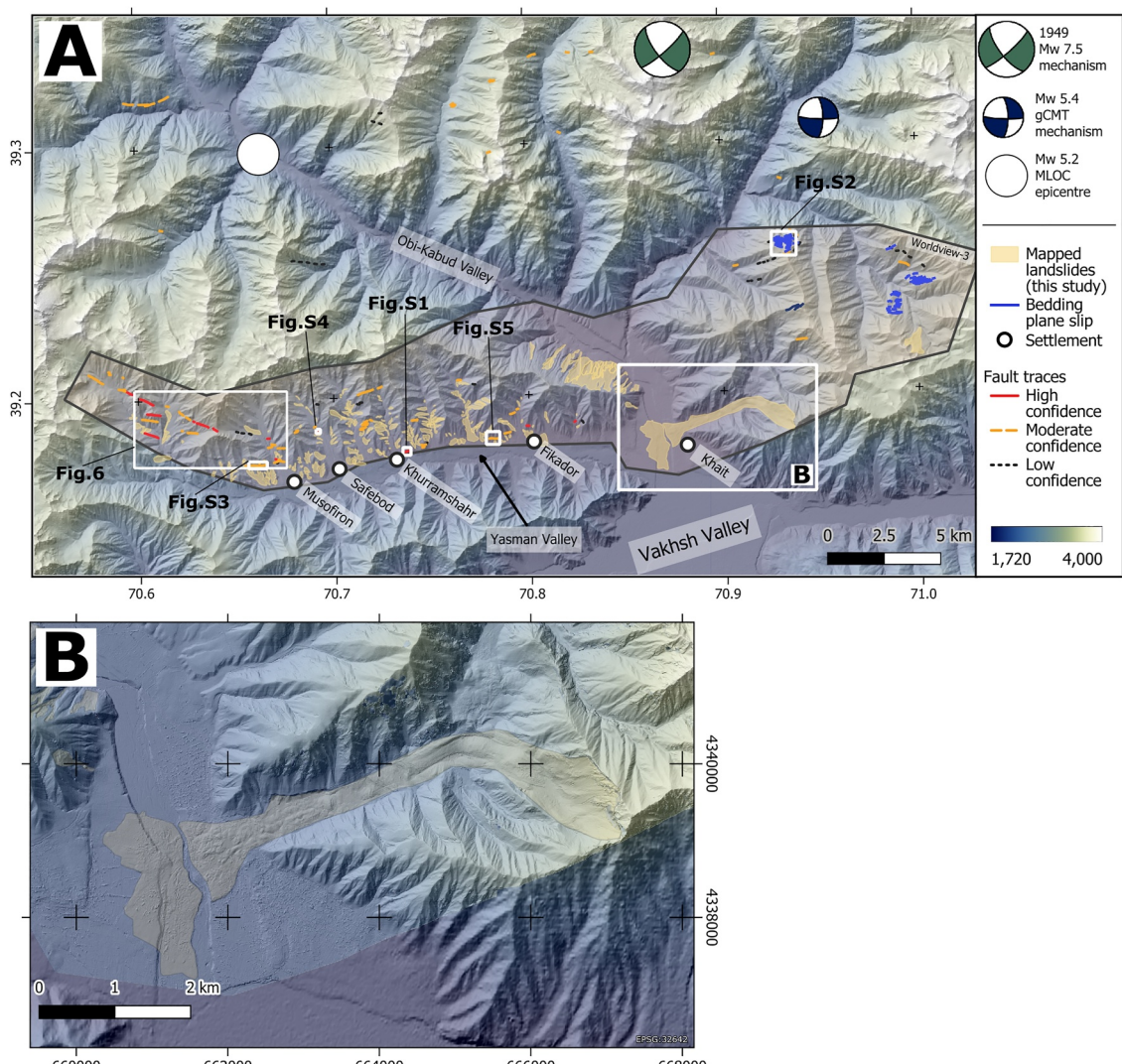


Figure 5. (a) Mapped surface ruptures in the Vakhsh Valley. *mloc* relocated earthquakes are shown, including the M_w 7.4 1949 Earthquake, these indicate the site of rupture initiation. The focal mechanism provides an average radiation pattern for the duration of the earthquake. The Worldview 3 0.3 m satellite imagery and DEM is shown by the pink polygon. Within this we mapped surface ruptures, categorized into confidence levels, and mapped recent landslides. We observe clear surface ruptures in the western end of the Vakhsh valley and can trace these east along the northern side of the valley to the town of Khait. East of Kahit, we find parallel scarps which may be bedding plane slip or sackungen (Figure S2 in Supporting Information S1). (b) Close up of the Khait landslide, triggered by the 1949 Earthquake, which covered large parts of the towns of Khait and Khisorak.

For Agisoft Metashape, we aligned the images using the in-build RPCs. To optimize the camera model we filtered the resulting tie points, removing the poorest 10% of points according to the Gradual Selection function. Having filtered the tie points, we used the Optimize Cameras function to improve the camera model. After that we built the point cloud and constructed the DEM from this. The point cloud was not filtered further, and the DEM's horizontal resolution is 1 m.

For Ames Stereo Pipeline, we first orthorectify the raw stereo images using the JAXA AWd30 Digital Elevation model (Tadono et al., 2014; Takaku et al., 2014). This removes most of the disparity from the image pair, and allows us to use a smaller search area when correlating features between images, increasing reliability and reducing computing time. We then use ASP's MGM algorithm with a 7×7 correlation kernel and subpixel refinement to determine the remaining distortion in the images. The result is then gridded to 0.5 m resolution and smoothed using a 9×9 pixel median filter, and outlier point removal based on triangulation error (see Appendix E for processing parameters). For regions of particular interest, we rerun the above at 0.3 m resolution. We project

Table 2
mloc Relocated Events

Event number	Date	Time	Lon	Lat	Depth	Strike	Dip	Rake	Magnitude	Depth constraint	Calibration code
1	10/07/1949	03:53:37	70.87061	39.3366	22	50	80	-20	7.6 Mw	1	CH04
2	10/07/1949	14:13:21	71.26403	38.9969	10	-	-	-	5.0 ml	c	CT04
3	10/07/1949	15:49:13	71.39584	39.21076	20	-	-	-	6.7 MS	1	CH04
4	10/07/1949	16:24:01	71.10634	39.25517	20	-	-	-	6.5 Ms	1	CH05
5	14/04/1951	04:10:06	71.65266	39.11131	15	-	-	-	-	n	CH04
6	12/05/1951	22:07:52	71.35382	39.55589	15	-	-	-	5.3 MS	1	CH06
7	18/08/1954	23:32:11	70.67238	39.11505	15	-	-	-	-	1	CH05
8	15/06/1955	01:03:56	71.57675	39.17804	15	-	-	-	5.2 MS	n	CH05
9	11/04/1956	01:45:12	70.38085	38.88154	15	-	-	-	-	n	CH05
10	13/01/1957	11:38:17	70.60721	38.789	10	-	-	-	-	n	CH03
11	07/01/1958	06:05:09	70.40051	38.92502	10	-	-	-	-	n	CH02
12	31/07/1959	19:53:03	70.48573	38.89856	10	-	-	-	-	n	CH02
13	16/03/1963	22:28:50	71.77883	39.08796	54	-	-	-	-	1	CH03
14	24/10/1964	06:50:56	70.76353	38.68794	15	-	-	-	-	1	CH04
15	25/10/1964	22:56:05	70.77611	38.69069	28.7	-	-	-	-	n	CH04
16	02/12/1964	12:31:40	70.66577	38.90327	33	-	-	-	4.7 mb	n	CH07
17	11/04/1966	16:42:50	70.61553	39.00357	10	-	-	-	-	n	CH04
18	14/04/1966	21:06:14	70.59585	38.94022	10.3	-	-	-	-	n	CH03
19	06/07/1966	11:57:22	71.3672	39.04672	15	-	-	-	-	1	CH05
20	08/09/1967	05:23:40	70.48121	38.45464	12	-	-	-	4.9 mb	1	CH05
21	22/03/1969	04:52:33	70.56975	38.93353	10	-	-	-	5.3 mb	n	CH03
22	27/03/1969	11:19:25	71.81149	39.1282	20	-	-	-	4.9 mb	1	CH04
23	27/03/1969	19:37:41	71.81734	39.16763	20	-	-	-	4.6 MS	1	CH04
24	09/10/1970	13:48:47	71.53075	39.19212	10	-	-	-	-	1	CH03
25	08/12/1970	11:53:14	70.29964	38.8334	10	-	-	-	4.5 mb	n	CH06
26	03/01/1973	14:31:02	71.8851	39.17562	27.4	-	-	-	5.5 mb	n	CH02
27	03/01/1973	15:05:12	71.90237	39.1811	20	-	-	-	4.8 mb	1	CH06
28	13/09/1973	06:40:33	70.55489	38.93078	9.2	-	-	-	4.5 mb	n	CH04
29	29/12/1974	04:59:01	71.67186	39.24657	15	-	-	-	5.2 MB	1	CH03
30	09/06/1975	18:36:46	70.30393	38.90781	3.6	-	-	-	5.1 mb	n	CH03
31	02/10/1975	19:33:44	71.53063	39.20663	15	-	-	-	4.3 mb	1	CH04
32	10/07/1976	10:21:21	70.66452	39.29765	32	-	-	-	5.2 mb	c	CT03
33	03/09/1976	21:52:41	70.71432	38.9613	9.9	-	-	-	5.1 mb	1	CH03
34	01/06/1977	20:07:26	70.24838	38.67493	0	-	-	-	4.5 MB	1	CH05
35	20/06/1977	03:07:38	71.22997	38.96185	0	-	-	-	4.5 MB	1	CH06
36	25/12/1977	16:18:50	70.70458	38.94938	2.9	-	-	-	5.4 MB	n	CH04
37	15/06/1978	17:00:06	71.64034	39.30632	33	-	-	-	4.9 MB	c	CT04
38	26/09/1978	19:21:46	70.76115	38.99837	10	-	-	-	5.1 MB	1	CH03
39	30/12/1978	05:06:54	70.58215	38.50185	10	-	-	-	4.9 mb	1	CH03
40	16/04/1979	04:56:17	70.58546	38.86304	11.9	-	-	-	4.8 MB	c	CT05
41	20/10/1979	19:40:39	70.61967	39.01075	13.4	-	-	-	4.7 mb	1	CH03
42	17/01/1980	22:47:13	71.6597	39.29582	3	-	-	-	5.0 MB	c	CT05
43	19/03/1981	09:59:44	70.33974	38.9182	3	-	-	-	4.7 Mb	1	CH03

Table 2
Continued

Event number	Date	Time	Lon	Lat	Depth	Strike	Dip	Rake	Magnitude	Depth constraint	Calibration code
44	14/04/1981	03:03:00	71.63194	39.10764	20	—	—	—	5.1 Mb	c	CT05
45	23/02/1982	21:09:49	71.92982	39.31759	33	—	—	—	4.8 MS	d	CH04
46	15/04/1982	16:15:35	71.75262	39.41529	20	—	—	—	4.7 Mb	c	CT05
47	06/04/1983	22:18:44	71.42824	38.896	5	—	—	—	5.3 Mb	l	CH02
48	01/10/1983	07:15:16	70.49506	38.83492	3	—	—	—	4.9 Mb	n	CH03
49	19/02/1984	13:57:50	70.43224	38.95599	3	—	—	—	4.5 Mb	c	CT05
50	26/10/1984	20:22:18	71.33522	39.25227	3	37	77	9	6.1 Mw	l	CH02
51	26/10/1984	21:33:34	71.3146	39.25652	3	—	—	—	5.1 Mb	l	CH03
52	27/10/1984	00:47:30	71.4117	39.24921	34	—	—	—	4.3 Mb	c	CT04
53	30/10/1984	22:55:24	71.29742	39.27645	43	—	—	—	4.8 Mb	c	CT05
54	06/01/1985	01:06:10	71.33633	39.22615	10	—	—	—	4.7 Mb	n	CH02
55	16/03/1985	09:12:45	71.39088	39.25253	3	—	—	—	5.1 Mb	n	CH02
56	01/10/1985	17:17:55	70.47604	39.25897	3	—	—	—	5.0 Mb	n	CH03
57	31/10/1986	11:24:37	71.40377	39.24342	15.4	—	—	—	4.8 Mb	n	CH03
58	23/02/1987	00:21:17	70.61222	38.99633	3	173	55	36	4.9 Mw	l	CH03
59	17/07/1987	17:23:23	70.70097	38.95215	3	—	—	—	5.0 Mb	l	CH04
60	21/12/1987	04:28:23	70.74636	38.84312	3	—	—	—	5.1 Mb	l	CH02
61	09/01/1988	03:55:01	71.50925	39.17878	3	275	41	148	5.1 Mw	l	CH02
62	10/01/1988	02:34:35	71.52753	39.18367	10	—	—	—	4.8 Mb	c	CT03
63	28/01/1988	18:05:56	71.90644	39.20758	3	—	—	—	4.7 Mb	l	CH02
64	16/05/1988	06:05:41	71.20319	39.25649	29.6	—	—	—	4.7 Mb	c	CT04
65	30/05/1988	20:48:51	71.13059	39.25717	3	—	—	—	4.5 Mb	c	CT05
66	10/06/1988	21:11:13	71.66122	39.26106	3	—	—	—	5.1 Mb	c	CT03
67	20/09/1988	14:41:39	71.37408	38.54937	3	—	—	—	4.8 Mb	l	CH03
68	03/10/1988	00:24:46	70.75941	38.75999	3	—	—	—	5.0 Mb	l	CH02
69	14/12/1988	11:45:55	71.75731	39.30695	3	3	51	127	5.3 Mw	l	CH02
70	03/05/1989	19:59:16	70.72493	39.05821	3	—	—	—	5.1 Mb	l	CH02
71	01/07/1989	18:27:09	71.55833	39.21179	10	—	—	—	4.9 Mb	c	CT03
72	06/11/1989	19:42:31	71.65889	39.31899	3	—	—	—	5.1 Mb	l	CH04
73	30/09/1990	21:22:58	70.90736	38.9707	3	—	—	—	5.2 Mb	l	CH02
74	03/11/1990	16:39:51	71.39521	39.11377	3	215	33	67	5.4 Mw	l	CH02
75	11/11/1990	03:19:41	71.8169	39.33453	3	—	—	—	5.3 Mb	c	CT03
76	26/02/1991	07:28:42	71.62002	39.36655	10	—	—	—	4.9 Mb	c	CT04
77	03/03/1991	18:08:59	71.63497	39.2776	3	—	—	—	5.3 Mb	c	CT02
78	26/04/1991	22:24:00	70.95485	39.02845	10	193	43	46	5.2 Mw	l	CH02
79	11/01/1992	20:09:18	70.60247	38.86383	16.6	—	—	—	4.8 mb	l	CH03
80	27/12/1992	21:09:35	71.74422	39.63576	33	—	—	—	5.0 Mb	c	CT04
81	08/08/1993	22:41:42	70.4263	38.68899	3	—	—	—	4.9 mb	c	CT04
82	02/10/1993	01:17:29	70.00493	39.06828	14.2	—	—	—	5.0 mb	c	CT04
83	10/02/1994	02:24:34	71.59596	39.2171	10	—	—	—	5.1 mb	c	CT04
84	01/05/1994	21:17:17	71.6433	39.25938	16	1	24	60	5.2 Mw	c	CT03
85	04/05/1994	10:40:12	70.30777	38.89116	9.6	—	—	—	4.6 mb	c	CT04
86	10/06/1994	03:00:42	70.55871	38.77624	16	—	—	—	5.2 mb	c	CT03

Table 2
Continued

Event number	Date	Time	Lon	Lat	Depth	Strike	Dip	Rake	Magnitude	Depth constraint	Calibration code
87	20/02/1995	04:12:23	70.95072	39.30802	20.2	1	71	-6	5.3 Mw	d	CH03
88	23/11/1996	01:56:53	70.76528	39.04081	15	-	-	-	4.7 mb	c	CT04
89	05/03/1998	23:58:40	71.63692	38.89764	17.6	-	-	-	5.1 mb	c	CT03
90	23/03/1998	10:11:49	70.74047	38.93106	15	-	-	-	4.3 mb	c	CT05
91	14/06/1998	14:12:04	70.20366	38.67724	10.6	-	-	-	4.5 mb	d	CH05
92	11/09/1998	05:53:49	70.33167	38.84949	35	-	-	-	4.7 mb	c	CT03
93	22/09/1998	01:08:21	71.41234	39.11301	15	-	-	-	4.6 mb	c	CT04
94	13/07/2003	14:36:15	70.56624	38.8916	32	-	-	-	4.7 mb	c	CT04
95	20/10/2004	11:57:49	70.47137	38.55699	0	-	-	-	5.2 mp	c	CT02
96	17/11/2004	07:34:25	71.73488	39.26509	33	195	83	4	5.1 Mw	c	CT03
97	17/11/2004	20:58:19	71.80075	39.24652	14	185	88	-1	5.8 Mw	c	CT02
98	18/11/2004	02:30:35	71.77162	39.22501	10	49	75	-5	5 Mw	c	CT02
99	18/11/2004	21:18:52	71.8633	39.17276	0	201	63	18	4.8 Mw	c	CT02
100	21/11/2004	20:45:20	71.77027	39.19962	0	322	42	-105	5 Mw	c	CT02
101	06/07/2006	03:57:50	71.79269	39.16844	0	283	59	146	5.8 Mw	d	CH02
102	02/02/2007	22:02:42	71.33539	39.07028	0	213	45	58	5.2 Mw	c	CT02
103	31/07/2007	02:47:05	71.34367	39.1237	16	50	41	83	5 Mw	d	CH03
104	29/09/2008	13:15:13	70.29797	38.86585	7.4	-	-	-	3.8 mb	n	CH02
105	13/10/2008	17:16:09	70.35134	38.69936	10.4	47	28	128	5.3 Mw	1	CH02
106	13/10/2008	17:35:44	70.34377	38.72358	10.4	-	-	-	4.2 mb	1	CH02
107	25/05/2009	15:18:52	70.57591	38.85828	12.6	-	-	-	4.8 mb	m	CH02
108	26/08/2009	07:26:37	70.65869	38.96666	12.3	83	79	178	4.9 Mw	m	CH02
109	13/10/2009	12:47:15	70.7757	38.72603	14.8	47	86	3	5.1 Mw	m	CH02
110	02/01/2010	02:15:04	71.45055	38.28074	7.3	232	58	-24	5.5 Mw	m	CH02
111	14/02/2010	20:32:43	71.73	39.70472	13.7	-	-	-	4.0 mb	m	CH02
112	21/02/2010	02:05:18	71.44749	38.24696	8.6	-	-	-	3.9 mb	m	CH02
113	28/02/2010	01:01:31	71.43404	38.29802	6.4	-	-	-	4.3 mb	m	CH02
114	25/04/2010	01:13:54	71.45145	38.24351	7.2	-	-	-	3.7 mb	m	CH02
115	14/05/2010	07:02:08	71.42536	38.31184	5.7	-	-	-	4.0 mb	m	CH02
116	04/07/2010	01:56:47	70.34364	38.85169	0	-	-	-	4.4 mb	1	CH02
117	20/08/2010	16:57:13	71.82544	39.30531	0	-	-	-	5.3 mb	1	CH02
118	07/10/2010	01:40:03	70.26825	39.22232	5	-	-	-	4.4 MS	1	CH02
119	09/10/2010	10:15:14	70.288	39.23854	10	-	-	-	4.7 mb	1	CH02
120	11/10/2011	01:17:14	70.57779	38.83686	0	-	-	-	4.8 mb	1	CH03
121	05/11/2011	03:22:26	71.78772	39.4027	12.8	-	-	-	4.3 MS	1	CH03
122	29/12/2011	15:27:17	70.72045	38.67907	42.4	-	-	-	4.3 mb	c	CT03
123	12/05/2012	23:28:41	70.35395	38.66795	0	-	-	-	6.8 mb	c	CT02
124	01/02/2014	08:31:17	70.5445	38.87171	10.1	-	-	-	4.1 mb	n	CH02
125	29/08/2014	01:03:59	71.5763	39.21823	15	92	61	156	4.9 Mw	1	CH02
126	01/10/2014	03:12:51	70.4751	38.87388	0	-	-	-	4.0 mb	1	CH03
127	20/05/2015	03:31:40	70.19637	38.64161	0	78	26	155	5.2 Mw	n	CH02
128	17/02/2016	23:58:01	71.42539	39.10115	24.3	-	-	-	4.4 mb	n	CH02
129	24/03/2016	08:37:34	70.70731	38.98664	17.3	-	-	-	4.8 mb	1	CH02

Table 2
Continued

Event number	Date	Time	Lon	Lat	Depth	Strike	Dip	Rake	Magnitude	Depth constraint	Calibration code
130	15/01/2017	13:18:09	70.76455	39.05527	12	–	–	–	4.4 mb	n	CH03
131	03/05/2017	04:46:53	71.40902	39.52523	0	–	–	–	4.5 mb	n	CH03
132	03/05/2017	04:47:11	71.47045	39.47744	5	–	–	–	6.4 MS	n	CH02
133	03/05/2017	20:03:10	71.50573	39.50698	5	–	–	–	4.6 MS	n	CH02

Note. Depth constraint codes: *c*: fixed at arbitrary depth; *d*: depth fixed with teleseismic depth phases; *m*: *mloc* solution with free depth; *n*: depth fixed using near source direct arrivals; *l*: depth fixed using local distance method (described in Section 3.2.3); Calibration code (how constrained is the location): CH01-best; CH05-worst.

the DEMs and orthoimages into the WGS84/UTM zone 42°N coordinate reference system (EPSG:32642) to allow us to make accurate meter-scale measurements.

For analysis of faulting we use the orthorectified optical imagery to identify surface ruptures and other features such as sag ponds and stream channel offsets not visible in the DEM. We use the DEM for measuring vertical offsets and providing constraint on the relative ages of geomorphic deposits cut by faults. The DEM also provide additional context for features whose interpretation is ambiguous based on orthophotos alone. We use the NIR band in the multispectral orthophotos to aid in linear vegetation patterns, potentially caused by lines of springs along faults. For measuring offsets we use the Measure Line tool in QGIS 3.28.3 (<https://doi.org/10.5281/zenodo.7575913>) using EPSG:32642 UTM Zone 42°N. We manually measure lateral offsets due to the high gradients on the surfaces and DEM noise which preclude use of automatic tools such as LaDiCaoz (Zielke & Arrowsmith, 2012). We estimate uncertainty by manually fitting the maximum and minimum possible offsets on streams using the orthoimagery (e.g., Figure 9). For vertical displacements we fit footwall and hangingwall surfaces using linear regression and use the difference in intercepts at the fault trace (Tsai et al., 2022).

Mapped active faults are assigned a confidence level (1 = high, 2 = moderate, 3 = low). High level confidence refers to linear traces that are clearly visible and are either associated with offset landforms, are nearby along strike of offset landforms, and may also be associated with springs. Moderate confidence indicates a linear feature which aligns with high confidence features. Low confidence features appear visually similar to faults, but may also align with bedrock geological structures and so scarps may relate to differential erosion of bedrock, rather than active faulting.

4. Results

4.1. Regional Seismicity and Source Parameters of the 10th July 1949 Khait Earthquake

We used digitized analog seismograms determine the source parameters of the 1949 mainshock as described in Section 3.1. We calculated surface wave, body wave and moment magnitudes of $M_s 7.8 \pm 0.4$, $M_B 7.6 \pm 0.2$, and $M_w 7.6 \pm 0.2$. These are slightly higher than previous magnitude estimates (see Table 1). Then we model the focal mechanism for the 1949 mainshock using amplitude ratios comparison of observed (digitized analog) and synthetic data. We find that the earthquake had a strike-slip mechanism of strike 50 ± 20 , dip 80 ± 10 and rake -20 ± 10 . The mechanism's PT axes show north-south compression: consistent with the pattern represented by other moderate magnitude earthquakes in the region, and agreeing with geological and geodetic observations of N-S compression (Leith & Alvarez, 1985; Metzger et al., 2020a, 2020b). The calculation were repeated for different test depths from 0 to 40 km with a step of 2 km, showing minimum misfit for the depth of 22–24 km. We improved the 1949 epicentral location, producing a catalog of 133 well located events within 1° distance of Khait, spanning 1949–2020, as described in Section 3.2.1 (Figures 2b and 5). These events are presented in Table 1. We find the 1949 mainshock occurred further north than previously reported, north of the Obi-Khabud valley (Figure 5a) at 39.3366°N , 70.8706°E . The formal uncertainties from MLOC are around ~ 5 km, but this represents a lower bound. The initial estimation of the source time duration for the Khait earthquake was derived from the P-wave duration observed in teleseismic records from European stations. The P-wave records for the Z components of these European stations (refer to Figure 3b) were aligned and stacked to create a normalized summation trace (SUM_Z, as shown in Figure 3b, top). This stacked trace indicates that the source duration is between 25 and 35 s (highlighted in red). A visual inspection of the trace does not reveal a definitive single value for the source time

duration; therefore, we refer to it as a range. We will now describe the key patterns visible in the 133 well located earthquakes and discuss their significance.

In the western part of the cluster, the seismicity forms an ellipse with long axis roughly parallel to the Vakhsh valley (Figure 10a-1). In cross section, the earthquake hypocenters align along a plane dipping south at ~50° which intersects with the Vakhsh Fault plane at the surface. This alignment appears robust, as our depth errors are less than ~5 km and the focal mechanism planes align with We interpret the 50° plane as a thick-skinned component of thrusting. Focal mechanisms show right lateral oblique thrusting on planes striking WSW-ENE, sub-parallel to the Vakhsh Thrust surface trace. This sense of motion agrees with GNSS and InSAR data (Metzger et al., 2020a, 2020b, 2021).

Between (71°E, 39°N) and (71.3°E, 39°N) (Figure 10), where the Darvaz and Vakhsh faults converge, there is a ~30 km long region where we do not observe earthquakes (Figure 2b). This behavior may be due to lateral variability in the properties of the Vakhsh Thrust décollement, with varying proportions of seismic to aseismic slip. It may also be due to our catalog being incomplete and so not capturing the full earthquake cycle on all parts of the fault.

East of this, at (71.4°E, 39.1°N) (Figure 10a-2), there are three thrust mechanisms, striking northeast-southwest, one of which occurred in 1990 (M_w 5.9) and two in 2007 (M_w 5.5 and M_w 4.9). These are collocated with a linear east-west earthquake rupture visible in open-source imagery. We acquired a polygon of Pleiades imagery to investigate these ruptures (Figure 8, Section 4.2.1).

Further east, there are two distinct groups of earthquakes. One group (center 71.6°E, 39.2°N) (Figure 10a-2) trends northeast, and appears to be the continuation of the three thrusts discussed above. The mechanisms are oblique left-lateral thrusts. The other group (center 71.7°E, 39.2°N; Figure 10a-3) trends north-south is predominantly right-lateral strike slip earthquakes, but also contains both a reverse and normal earthquake. Taken together with the wide range of geologically-derived PT axis orientations in this area (Kufner et al., 2018), these mechanisms indicate a complex zone of faulting likely due to the intersection of the Vakhsh, Darvaz and Pamir Frontal Thrust Faults.

At the confluence of the Kyzyl-su and Muksu rivers (71.4°E, 39.2°N; Figure 10a-4) there is an alignment of epicenters trending WNW for ~50 km from the Vashkh river valley in the east, to the 1949 mainshock at its western end. The three largest earthquakes in the group are the 1949 M_w 7.6 earthquake, and the two largest aftershocks which occurred on the same day MS6.7 and MS6.5. These are followed by a sequence which unfolded over the period 1984–88, culminating with an earthquake in 1995 that is SE of the 1949 event. This alignment in seismicity may represent activation of a tectonic structure, the full length of which was activated in 1949. We were not able to find surface ruptures in the open-source imagery, though this was either low resolution or obscured by snow.

4.2. Geomorphology of the 1949 Khait Epicentral Zone

In this section we assess geomorphic evidence for active faulting, both along the Vashkh fault itself, and also in the regions surrounding our relocated epicenter and in the regions of highest seismic intensity (Figure 2a). We analyse digital elevation models (DEMs) derived from 70 cm Pleiades optical satellite data along the Vashkh fault (region shown in Figure 8) and 30 cm Worldview three optical imagery on the north-side of the Yasman valley, where the largest macroseismic intensity was observed (Figure 6).

4.2.1. Vakhsh Valley

The Vakhsh Fault runs along the southern side of the Vakhsh Valley and is left-stepping. Large scale dip-slip offsets are visible, likely accumulated over many earthquake cycles (Figure 2c). Past literature has proposed the 1949 Khait Earthquake was hosted on the Vakhsh Fault. We examined the region between the Muksu River and the Obikhingou River (Figure 2c) using Open-Source imagery for signs of single-event earthquake ruptures consistent with this. We identified two possible sites and acquired high-resolution satellite imagery over the most promising of these. This was then used for 0.5 m DEM construction. For the other sites we rely on freely available 30 m DEMs and Open Source Imagery.

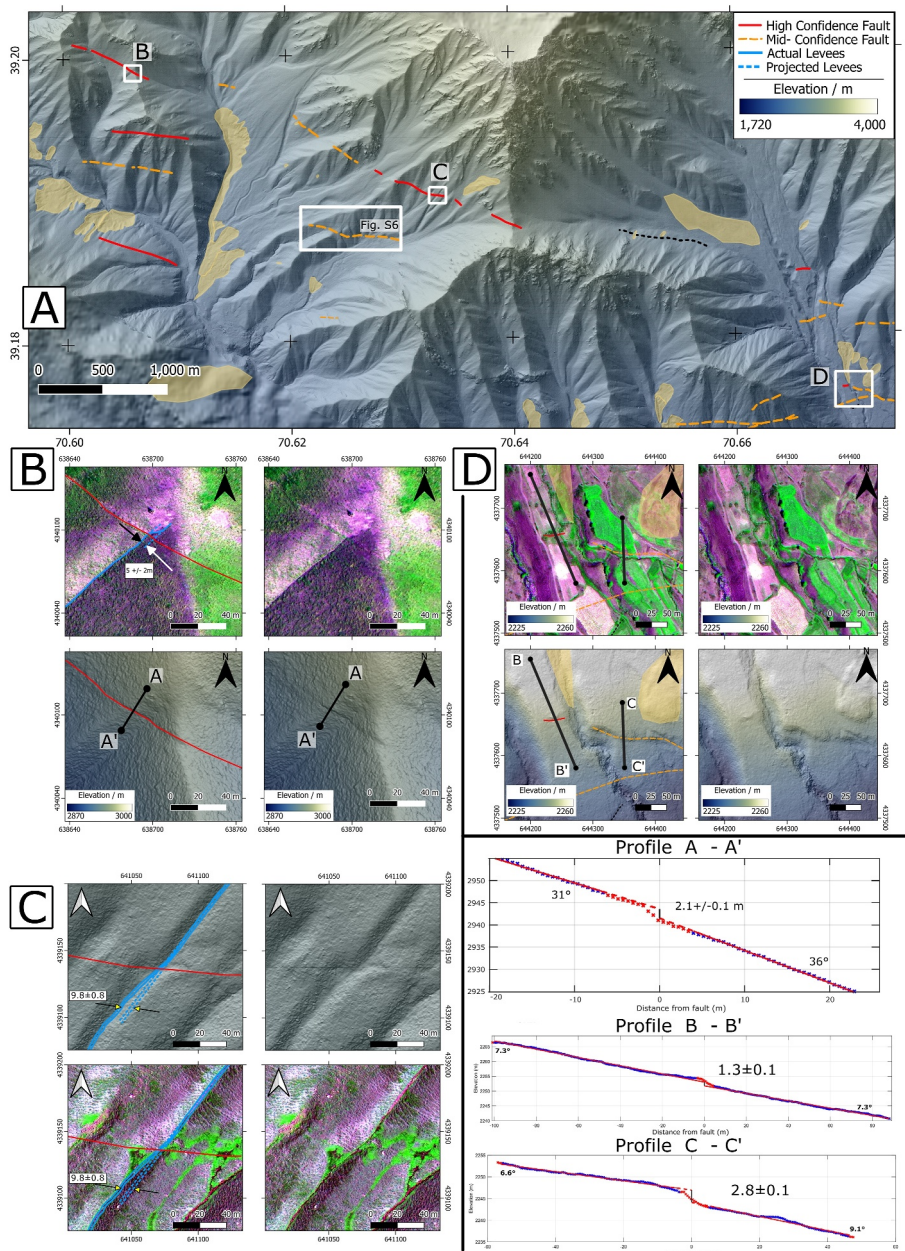


Figure 6. (a) Dip-slip and right-lateral strike-slip ruptures in the upper western end of the Yasman Valley. We observe a scarp crossing a wine-glass shaped drainage at (39.1991°N, 70.6059°E), which is not deflected by topography, implying a near-vertical fault dip. This crosses a smaller drainage showing a 5 m right-lateral stream deflection (b). In the hill-shaded DEM we measure a scarp with 2.1 m vertical separation (profile A-A') in the western wall of the drainage consistent with a near-vertical right-lateral fault. Further east, at (39.18999°N, 70.63390°E) we observe a scarp in the hillside, picked out by the areas of high Near-Infrared (green) in the false color images (c). We interpret this to mark vegetation along springs associated with the fault. By projecting stream levees downhill we measure a right-lateral stream deflection of 9.8 m. Finally, at (39.17609°N, 70.67037°E) north of the village of Musofiron, observe a scarp running across two different surfaces (d). Along profile B-B' we measure 1.3 m dip slip offset and along C-C', we measure 2.8 m dip-slip displacement. The disparity between these offsets may be due to C-C' scarp being modified to make the field boundary and canal, or could represent multiple earthquakes. The surfaces for profile B-B' and profile C-C' are less than 10° so in this case vertical separation is approximately equal to vertical tectonic offset.

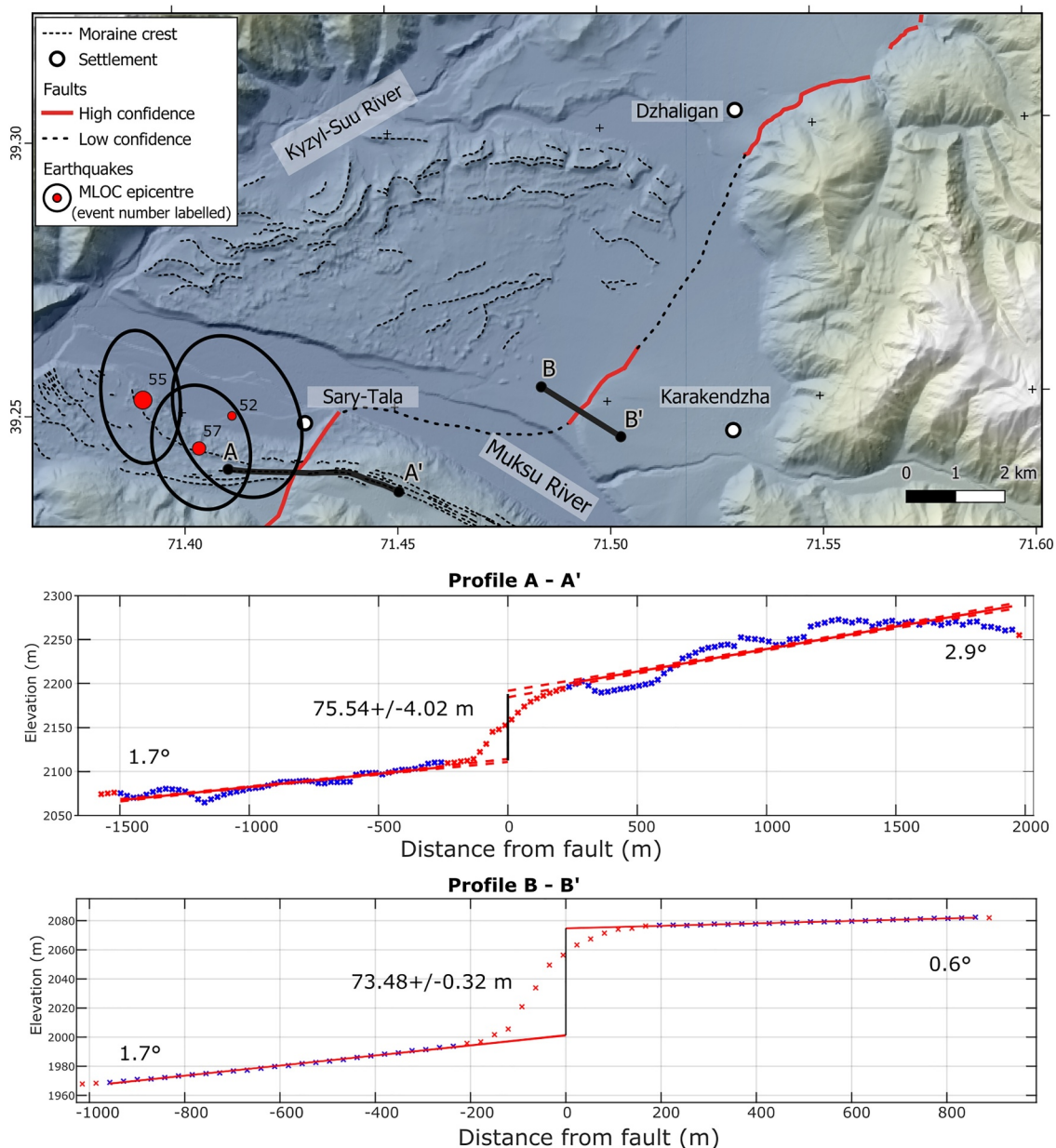


Figure 7. Last Glacial Maximum (LGM) moraine complex near Dzhaligan with dip slip offsets on both sides of the Muksu River. Profile A-A' shows lateral moraines dated to ~18 kyr by Grin et al. (2016) are offset with ~75 m vertical separation on the south side of the river and the fault zone is ~200 m wide. Profile B-B' shows a similar magnitude vertical separation in a fan deposit which postdates the LGM situated north of the Muksu River, with a fault zone ~300 m wide. The geomorphic surfaces on are near-horizontal for both offsets, meaning vertical separation should correspond to the vertical component of the tectonic offset. Taking together the age of the surfaces and the vertical tectonic offset, we can calculate a slip rate on this fault of ~5.5 mm/yr assuming a 50° dip suggested by earthquake depths and mechanisms (Figure 10). We interpret this to be a continuation of the Vakhsh/Darvaz Faults which joins up to the Pamir Frontal Thrust near Dzhaligan. Three earthquakes 4.3–5.1 m_B close to the offset further imply a tectonic origin for the offsets. Topography is from the ALOS AWD 30 m Global DEM.

Firstly, we identify two scarps that displace lateral moraines near Sary Tala (71.429°E, 39.246°N) and alluvial fans near the Karakendzha (71.494°E, 39.250°N) (Figure 7). The heights of these scarps are very similar: 76 ± 4 m at Sary Tala and 74 ± 1 m near Karakendzha, implying the two displacements formed by a fault which bends/steps east as it crosses the Muksu River. The moraines at Sary Tala are aged ~18 kyr according to cosmogenic exposure dating of boulders (Grin et al., 2016). The alluvial fans near Karakendzha have not been dated, but must be younger than the Sary Tala moraines assuming the scarp began growing after the glacier retreated. The Karakendzha alluvial fan offsets peter out north-westwards, possibly due to sedimentation from the

Dara River. However a scarp becomes clear again near the town of Dzhaligan where it bounds the mountains from the Kyzyl-Suu river valley. This continues eastwards and presumably joins the Pamir Frontal Thrust.

We also identify active fault traces within a glacial moraine complex on the south side of the Vakhsh valley. The moraines are cut by scarps younger than the LGM (~ 17 ka). We acquired 0.5 m Pleiades imagery and DEMs over this area (Figure 8). It is within a high valley $\sim 1,000$ m above the Vakhsh Valley floor and divides the Peter I Range and the wider Pamir mountains. This site contains the divides between three major catchments, with rivers flowing into the Musku River (east) the Vakhsh River (north) and into the Obikhingou River (west). At the base of the valley are a complex of glacial moraines, fed in the past by three small glaciers to the south. During the LGM, these glaciers likely filled this small valley and flowed into the Obikhingou catchment. Evidence for this is a WSW-oriented lateral moraine pair perched in the Obikhingou Catchment at (71.199°E, 39.033°N). Today, we observe a complex set of glacial moraines in the flat valley, representing about nine advances. These glacial deposits are cut by linear scarps which are co-located with thrust earthquake mechanisms described in Section 4.1 (Figure 10a-2).

We identify a prominent east-west scarp traversing undulating but overall low-relief glacial terrain. It is continuous for ~ 10 km and has a straight trace even across highly undulating ground, suggesting a steeply-dipping (near vertical) planar slip surface. It contains both up- and downhill facing scarps, and a right-stepping en-echelon arrangement of scarps suggestive of a near-vertical strike-slip fault (McCalpin, 2009). However, direct lateral offsets of gullies and ridge crests are not clear. The scarps traverse multiple generations of moraine deposits. They are clearly expressed in the youngest geomorphic surfaces and are higher in older moraines (Figure 8). Two possible interpretations for these scarps exist. One is that they are backthrusts of the Vakhsh Thrust, as in Schultz (2000), where overburden of the fold and thrust belt forces a gravitational collapse in the back of the fold. This could be aided by the steeply dipping bedding of the geology in the area. Another possibility is that they are a thrust-termination of the Darvaz Fault. As the left-lateral Darvaz fault bends from a NE-SW orientation to an E-W orientation, an unchanged slip vector would result in a change from strike-slip to thrust motion.

The final example of recent scarps is further west at (70.8125°E, 39.0256°N) (Figure 9). The hillslopes here are dissected by numerous short but prominent scarps. The scarps are short, linear and present in subparallel sets of ~ 20 . They frequently appear at the base of steep triangular facets, whose aspect appears approximately parallel to bedding planes. We interpret most of the scarps as landslip scarps. There are, however, some more laterally continuous scarps, that may have a tectonic origin, and these are mapped in red in Figure 9.

To conclude, although we find abundant evidence for post-glacial fault slip along the south side of the Vashkh fault, we find limited evidence of recent earthquake scarps developed on the fault. It is possible, at least along some sections, that the steep topography and extensive landsliding has erased all traces of the 1949 earthquake. However, considering the geodetic evidence for creep, the presence of evaporites in the fault, and the lack of mapped coseismic landsliding, we believe it unlikely the Vakhsh Fault ruptured in the 1949 earthquake.

4.2.2. Yasman Valley

The Yasman Valley is a tributary leading into the Vakhsh Valley, west of Khait (Figure 2). It is the site of highest reported damage and landsliding. We find compelling evidence for recent active faulting and potential single-event surface rupturing along its northern side, over a distance of ~ 25 km. We also mapped landsliding which likely occurred post-1949 based on visual comparison of vegetation growth to the Khait landslide. We acquired 0.3 m Worldview-3 imagery with a near-infrared (NIR) band for observing vegetation which we used to map surface ruptures and generate a DEM for scarp height measurement.

The clearest evidence of surface rupturing is observed along a 3 km-long section at the westernmost end of the valley (Figure 6a), where stream channels and ridge crests show $\sim 2\text{--}5$ m of right-lateral displacement, and patches of vegetation retain evidence for recent displacement (Figures 7–10).

In Figure 6b we observe right lateral stream offsets of between 5 ± 2 m and 2.1 ± 0.1 m. The fault trace continues north-west, beyond the limits of Figure 6b to the next catchment (Figure 6a), cutting across topographic contours. This implies a steeply dipping fault. We map two more high confidence potential ruptures about 600 and 1,300 m further south (Figure 6a). Further east, we identify a scarp crossing a hill slope, and measure a 9.8 ± 0.8 m right-lateral stream deflection (Figure 6c). We measure this displacement by projecting the stream levees above the fault to below the fault, and measure the offset between the present and projected stream.

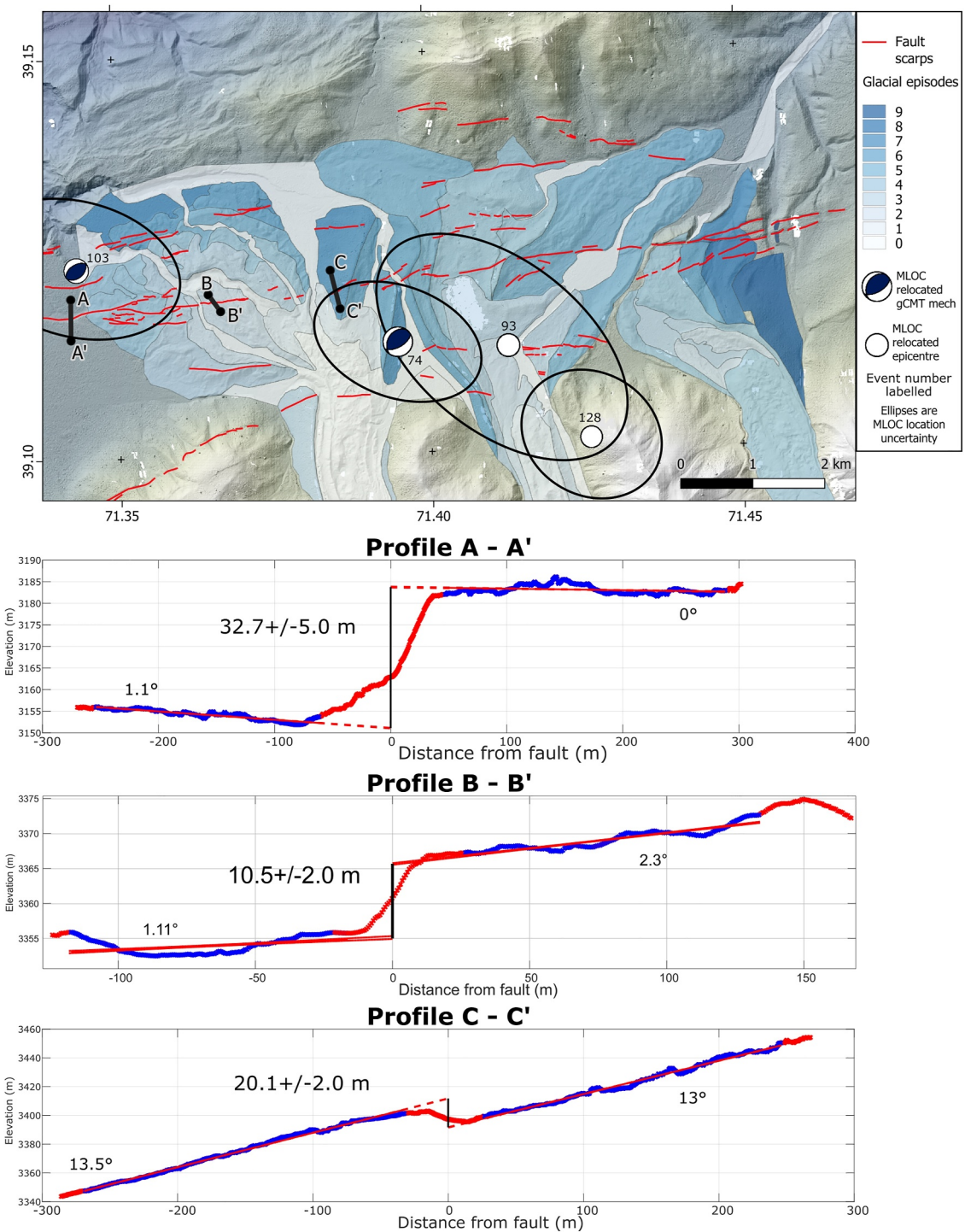


Figure 8. Pleiades-derived DEM showing glacial moraine complex on the south side of the Vakhsh Valley cut by linear, right-stepping scarps. There are progressive offsets in the older moraine sediments, implying multiple events on the fault. These scarps sit south of kilometer scale folding which is likely tectonic, and so we suggest are near-vertical splays whose motions do not reflect the underlying tectonic stresses. This is backed up by the *mloc* mechanisms which are relocated to beneath the scarps. Profile A-A' is in the oldest material, and shows vertical separation of ~ 33 m over a ~ 100 m interval; profile B-B' is in Unit 3, and shows vertical separation of ~ 10 m over an interval of ~ 20 m; and profile C-C' is in Unit 7 shows vertical separation of ~ 20 m over an interval of ~ 40 . Profiles A-A' and B-B' show downhill-facing scarps, whereas profile C-C' shows an uphill-facing scarp. Assuming the fault is near vertical, these measurements of vertical separation should correspond to tectonic offset.

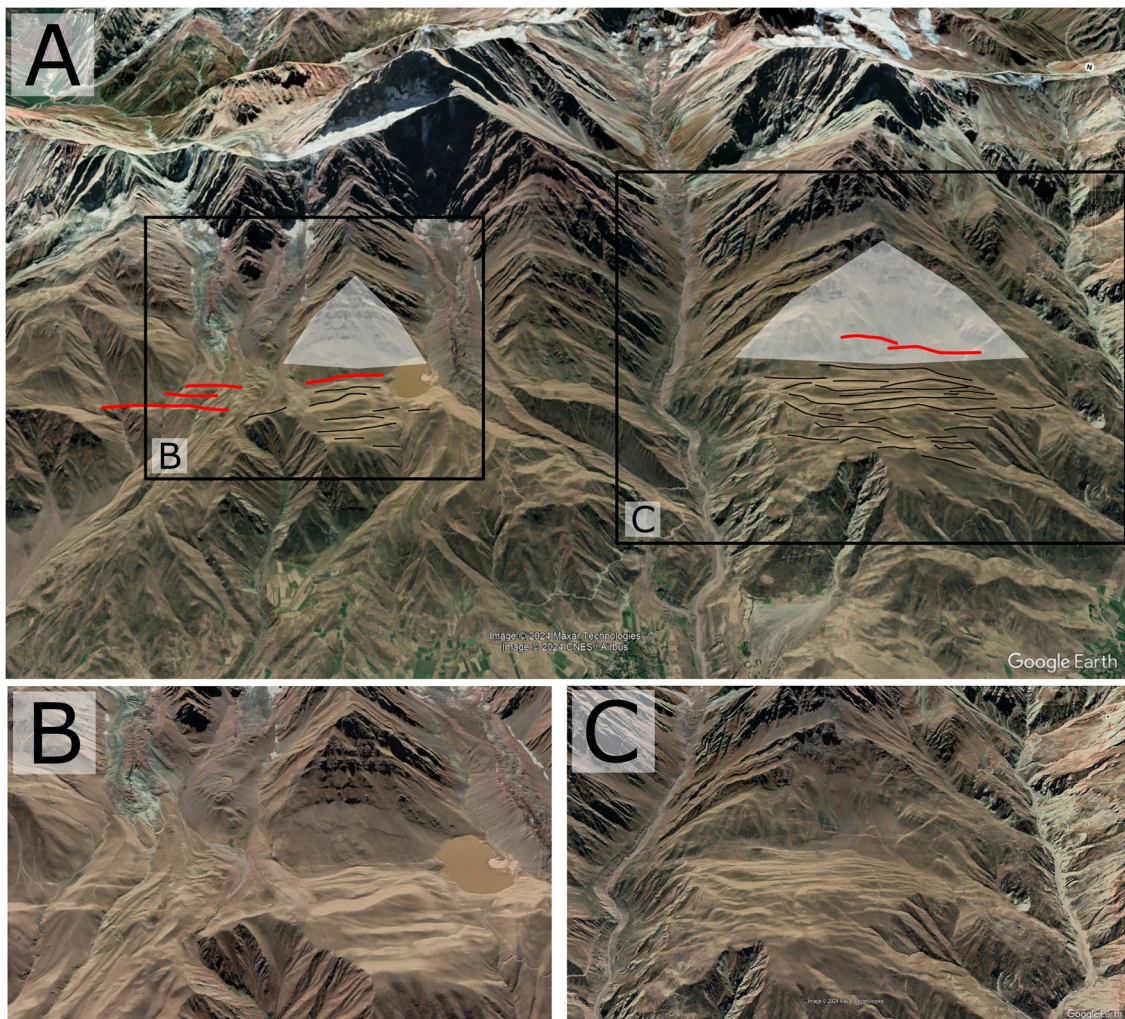


Figure 9. (a) South-facing perspective Google Earth Imagery of a section of the Vakhsh Valley showing surface ruptures likely not from the 1949 Earthquake (see Figure 2 for location). Interpreted tectonic surface ruptures are in red. Scarps associated with landsliding are in black. Triangular facets in white are interpreted as exposed planes along which slumping has occurred. (b) And (c) show uninterpreted close-ups of the boxes shown in (a).

Areas of high NIR (bright green) along the fault scarp represent vegetation, likely associated with a line of small springs. Further south, we observe a parallel alignment of springs, implying a parallel fault, but cannot identify any associated offset (Figure S6 in Supporting Information S1).

Near Musofiron, we observe a south-facing scarp modified along a field boundary (Figure 6d). The fields under cultivation show up as areas of high NIR (bright green), with a fallow field showing as pale purple near the bottom-center of the figure. A small landslide is visible in the top right of the figure. We measure a 2.8 ± 0.1 m dip-slip offset (profile C-C') where the scarp is part of the field boundary. To the west, across a stream, we observe a smaller 1.3 ± 0.1 m dip-slip offset (profile B-B'). It is possible that these two dip-slip measurements represent single and double event scarps, as the offset on profile B is approximately double that of profile B-B', though it is possible that the scarp height has been modified where it runs along the field boundary, and we have assigned only moderate confidence to this part of the fault. The stream which runs to Musofiron appears deflected ~ 25 m in a left-lateral slope, but we interpret this to result from the stream flowing around the raised field-boundary scarp, rather than a tectonic offset. On the hillside west of these examples, we observe fault traces of moderate confidence, as it is also possible that these are geological bedding planes (Figure S3 in Supporting Information S1).

Further east, near Safebod, we find a scarp with apparent dip-slip offsets of around 1.4 ± 0.2 m. This is sharp in the orthophoto but not visible in the hillshaded DEM. A small stream cuts the scarp at a $\sim 90^\circ$ angle, after which it

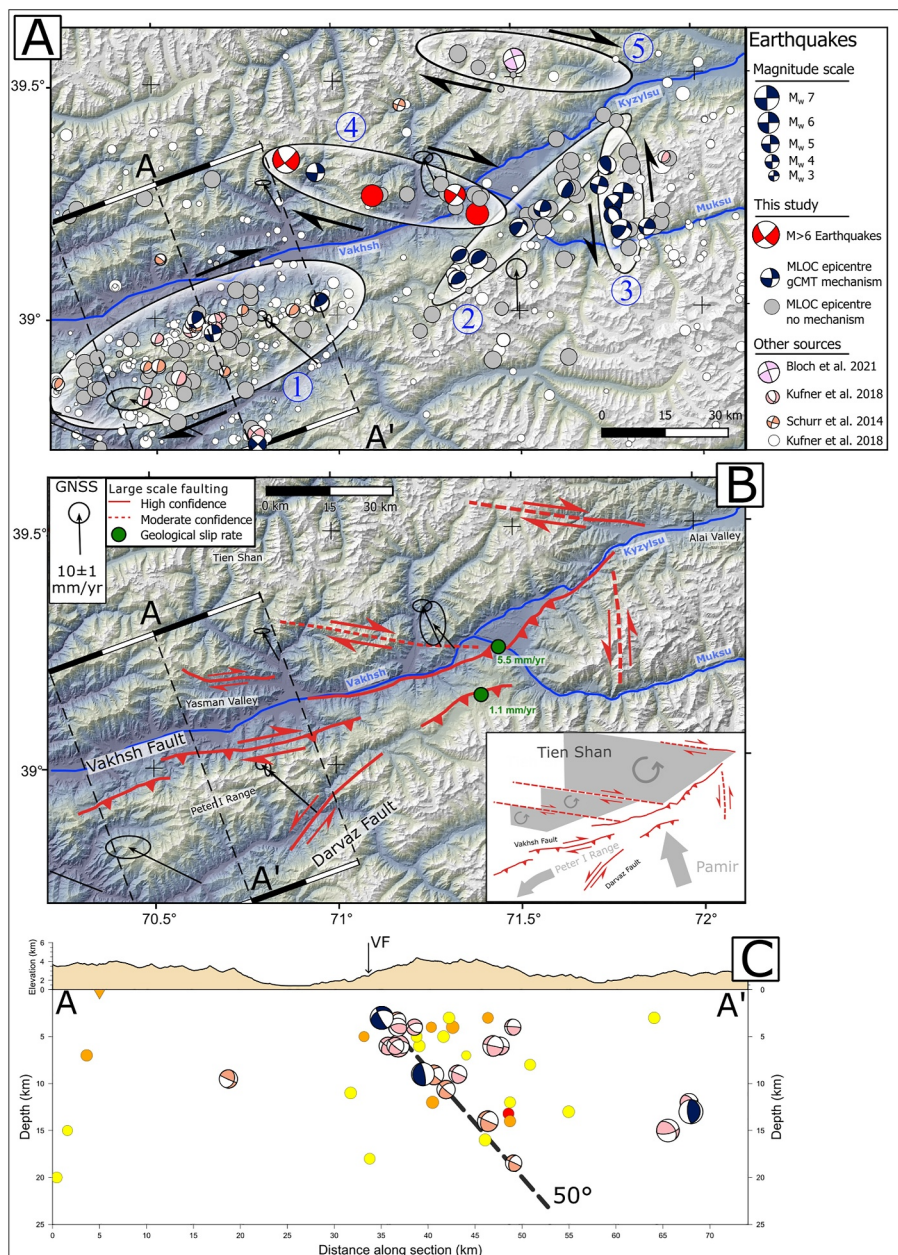


Figure 10. Interpreted version of Figure 2. (a) *mloc*-relocated epicenters and mechanisms grouped into clusters discussed in Section 5.1. (b) Interpretation of tectonic regime based on our relocated earthquakes and geomorphic mapping. High confidence faults are those for which we have geomorphic evidence, moderate confidence faults are those we have inferred based on epicenter and mechanism alignments. Geologic slip rate sites (green circles) suggest only half the geodetic slip rate is accommodated by the Vakhsh Fault. We suggest that in addition to the already known Vakhsh and Darvaz Faults, there exist a set of NW-SE trending right-lateral faults within the Tian Shan accommodating part of the convergence between the Pamir and Tian Shan. This is in contrast to previous tectonic models which localize this motion on the Vakhsh Fault. (c) Cross section showing *mloc*-relocated events. Epicenters with the better depth control are shown in hotter colors, and the uncertainty of depths is up to ~5 km. The alignment of hypocenters with mechanism focal planes suggests a fault dipping ~50° which connects to the surface trace of the Vakhsh Fault.

spreads out into several smaller channels (Figure S4 in Supporting Information S1). Near Khurramshahr, we observe a linear surface trace visible both in the elevation model and in the orthophoto. This scarp appears to offset a drainage ~6–12 m in a left-lateral sense, in the opposite sense to the examples described earlier. Here the

site interpretation is complicated by the presence of a recent landslide along-strike of the trace, and also by human modification, and we interpret the apparent left-lateral displacement as non-tectonic.

East of Khait the evidence for active faulting is less clear. We observe parallel scarps that follow topographic contours. These imply a moderate to shallow dip and align with bedding plane strikes in Soviet geological maps (Berezuk, n.d.). We therefore interpret them as slope failure scarps (sackungen). It is possible that they are simply scarps formed due to differential erosion of layers of variable resistance, though we would expect purely lithological scarps to be more laterally continuous.

5. Discussion

5.1. Causative Fault of the 1949 Earthquake

Our relocated 1949 epicenter is based on arrival time data, and thus locates the nucleation point of the earthquake. Together with macroseismic and landsliding data, our epicenter indicates the earthquake did not occur on the well-known Vakhsh fault, south of the Vashkh river, but on an unmapped fault within the Tian Shan basement north of the river. Surface rupturing has previously been difficult to map in the area due to inaccessibility and the steep, rapidly eroding landscape. The potential ruptures that we have identified from high-resolution optical satellite data are in the epicentral region, are relatively recent and have meter-scale lateral offsets along the Yasman Valley. This is consistent with the size and focal mechanism of the 1949 earthquake, though whether they were formed in the earthquake can only be resolved by detailed field study.

The 1949 Earthquake had a magnitude of M_w 7.6 (Table 1), equivalent to a scalar moment of $\sim 3.2 \times 10^{20}$ Nm. We have determined the hypocenter depth of 22–24 km using amplitude ratio comparison method. This is similar to the m_{loc} derived depth of 22 km (Table 1). However, the misfit function has demonstrated limited dynamics, suggesting that the method is not very responsive to the centroid depth. As a result, the issue of the certainty regarding centroid depth and the dependency of the scalar moment estimate emerges. Therefore, we conducted tests on the bias related to M_0 and magnitude using full-wavefield synthetics that were filtered with a standard Wiechert response for hypocenter depths between 10 and 30 km. Our findings revealed relative amplitude discrepancies of 1.1 for P waves on Z components and 1.3 for S waves on horizontal components. Consequently, we deduce that the uncertainties arising from the bias of the hypocenter and M_0 fall within a range of 0.1 for M_w , which lies within our M_w error estimate of ± 0.2 . We can now use this magnitude to estimate the length of the rupture.

Seismic moment is the product of the modulus of rigidity ($\sim 3 \times 10^{10}$ Pa), the area of the rupture plane, and the average amount of slip (Aki & Richards, 2002). For the down-dip width we assume a vertical fault and rupture of the entire seismogenic thickness of ~ 20 km based on the maximum depths from this study which is consistent with the base of crustal seismicity recorded by previous studies (Kufner et al., 2018; Schurr et al., 2014). Taking the slip measurement from satellite imagery of $\sim 5 \pm 2$ m (Figure 6b), we can then calculate a fault rupture length of 105 (+70/−30) km assuming vertical geometry. Another method to estimate fault rupture length uses the apparent P wave duration and assumes represents the apparent source time duration. The ~ 25 –35 s P-waveduration at stations in Europe (Figure 3b) suggests a 75–105 km end-to-end rupture length, assuming a typical rupture propagation speed of $\sim <3$ km/s (Bouchon et al., 2001), and up to ~ 150 –210 km if the rupture propagated bilaterally from the center of the fault. Super-shear rupture velocities >3 km/s are possible, but tend to occur only on straight, simple, well developed faults (Ansai, 2015), unlike the area where the 1949 earthquake occurred. Therefore, a total rupture length for the 1949 earthquake of ~ 75 –120 km is consistent with both estimation methods.

To the west of Khait we map ~ 25 km of surface ruptures in the Yasman Valley. East of Khait, we also map another ~ 10 km length of recent surface deformation, in addition to either bedding plane slip or sackung (Figure S2 in Supporting Information S1). We therefore assume that most of the fault rupture remains unidentified, either because it failed to break the surface, or has been removed from the landscape by landsliding.

Regional seismicity may help to determine the missing parts of the potential earthquake source. We observe a NW-SE alignment of epicenters and mechanisms, from the relocated 1949 epicenter in the NW to the confluence of the Musku and Kyzyl-Suu Rivers in the SE (71.35°E, 39.25°N) (Figure 10a–4), as discussed in Section 4.1. This alignment includes two major aftershocks which occurred on the day of the 1949 earthquake, and the focal planes of subsequent earthquakes align well with this epicenter alignment. This suggests part of the 1949 rupture occurred on a WNW-trend delineated by these earthquakes (Figure 10a–4). We are unable to see ruptures in this

area, however it is covered only by relatively coarse open-source imagery, and the terrain is extremely steep and prone to landsliding (Figure 2a): making it difficult to preserve ruptures.

Combining the observations, we infer that the 1949 Khait earthquake involved ~85 km length of predominantly right-lateral rupture within the Tian Shan. This included ~25 km length of rupture along the Yasman Valley, along which we see discontinuous surface rupture in satellite imagery, and ~50 km rupture on a separate WNW-trending fault from the confluence of the Muksu and Kyzyl-Suu rivers (Figure 10). The relocated 1949 epicenter is sited at the NW end of this second fault, and roughly mid-way along the total combined fault. Nucleation at the relocated epicenter implies a westward rupture propagation along the Yasman Valley and a ESE-ward propagation toward the river confluence. If we assume ~3 km/s rupture velocity, that implies a ~16 s source time function, which is similar to the ~20 s we estimate from P wave records in Europe (Figure 3).

These two parallel WNW ruptures match up with a set of ruptures and earthquakes that follow the same trend. The ruptures are at (71.8047°E, 39.5045°N) and the earthquake alignment is highlighted in Figure 10a-5. These faults bound blocks which accommodate N-S shortening by rotation on a vertical axis, playing a similar role to the much larger Dzungarian and Talas-Fergana faults (Figure 10b) (Campbell et al., 2013; Rizza et al., 2019).

5.2. Seismicity of the Vakhsh Fault

Our study finds little evidence for the Vakhsh Fault rupturing in the 1949 earthquake, with faults in the Tian Shan interior likely being responsible. This result then prompts the question of whether the Vashk fault has potential for producing significant earthquakes.

GNSS and InSAR (Metzger et al., 2020a, 2020b, 2021) velocity profiles across the Vakhsh Fault near Gharm show a steep gradient in fault-parallel velocity, implying shallow creep on the fault. However, fault perpendicular displacements have a much shallower gradient, and implies that thrusting is locked at depth. This is could be due to partitioning of strike-slip and thrust kinematics across different structures, analogous to the Main Recent Fault and the High Zagros Fault in Iran (Nissen et al., 2011).

The Vakhsh Fault itself evidently hosts moderate earthquakes up to M_w 5.9 (Figure 2b and Table 1). However, aside from the 1949 Earthquake we have no record of a $M_w > 7$ earthquake within ~200 km of Khait (Mikhailova et al., 2015). Either the historical catalog is incomplete, or the Vakhsh fault is incapable of hosting earthquakes this large. To better understand the behavior of the Vakhsh Fault further geodetic analysis is required. The terrain and snow cover makes small-baselines time series InSAR difficult (Metzger et al., 2021), so deploying dense arrays of GNSS stations or corner-reflectors for PS InSAR may be required to better understand the earthquake potential of the Vakhsh Fault.

On a regional scale, we propose a two-stage model of intramontane convergence between the Pamir and Tian Shan. In the first stage, the convergence is accommodated by simple underthrusting and subduction, as in the Alai Valley (Patyniak et al., 2021; Sobel et al., 2013; Zubovich et al., 2016). In the second stage, once all of the low-lying basin has been subducted (as it has near Khait), the kinematics change and shortening is accommodated by NW-SE striking right lateral faults, similar to the Dzungarian and Talas-Fergana Faults north of the Tian Shan (Rizza et al., 2019; Tsai et al., 2022) and the Kopeh Dagh Fault System in NE Iran (Hollingsworth et al., 2006). The Vakhsh Fault was likely site of this subduction in the past, analogous to the Pamir Frontal Thrust today. The relative convergence taken up by thrusting on the Vakhsh Fault and vertical axis rotations is unclear, and a question for future research.

5.3. Slip Rate of the Vakhsh Fault

We can estimate long term slip rate on the Vakhsh Fault by examining how glacial moraines are tectonically offset. In Section 4.2.1 we identified two areas where moraines are offset.

One site is on the banks of the Muksu River (ure 7) where lateral moraines of ~18 kyr age (Grin et al., 2016) are offset by 75.5 m. The alluvial fan on the north side of the river (deposited after glacial retreat) has a similar 73.5 m offset. Both surfaces are near-horizontal, so we can take the vertical separations observed in Figure 7 to be approximately equal to the vertical component of a tectonic offset on a dipping fault (Mackenzie & Elliott, 2017). This gives a vertical uplift rate of ~4.2 mm/yr, which projected onto a 50° dipping fault, as indicated by earthquake cross sections (Figure 10), would give a slip rate of 5.5 mm/yr.

The other site is situated in the Peter I Range (Figure 8) where we observe sub-vertical backthrust faults cutting a moraine complex we suggest is younger than the LGM (18 kyr) but for which we have no firm dating. Given the fault is near-vertical, we can again assume that vertical separation observed in topographic profiles is equivalent to the vertical component of the tectonic offset (Mackenzie & Elliott, 2017). If we assume the oldest mapped moraine coincides with the LGM, the offset since the LGM would be 20.1 m (Figure 8 profile B-B'), giving a vertical uplift rate of 1.1 mm/yr. If we assume instead the surface below the mapped moraines is coincident with the LGM, the LGM offset would be 32.7 m (Figure 8 profile A-A'), giving a vertical uplift rate of 1.8 mm/yr. This would give a fault slip rate of ~1.1–1.8 mm/yr.

To synthesize these results, we suggest that the Musku River site represents an estimate of the Vakhsh Fault and the Peter I site either represents movement on a backthrust (Schultz, 2000), or else a thrust-termination of the Darvaz fault. We therefore suggest the long term slip rate on the Vakhsh Fault is ~5.5 mm/yr. This is less than half the rate derived from geodetic estimates, which suggest >13 mm/yr present-day dip-slip strain accumulation on the fault (Metzger et al., 2020a). This adds to the evidence the Vakhsh Fault, rather than being the dominant structure taking up convergence between the Pamir and Tian Shan, is one of several structures around the Vakhsh Valley accommodating this convergence since the LGM.

5.4. Implications for Hazard in the Region

Determining the source of the 1949 Khait Earthquake and characterizing the earthquake potential of active faults in the region have a particular present-day relevance for earthquake hazard.

Hydroelectricity is the main source of electricity for Tajikistan, and the country exports this to its neighbors (IEA, 2022). Several hydroelectric dams have been built along the Vakhsh River, including at Nurek and Rogun (150 and 110 km from Khait respectively (Figure 1)). Further expansion of hydroelectricity requires an understanding of the distribution of tectonic deformation through the region and knowledge of earthquake-hosting faults. In the worst case, earthquake shaking and fault movement may present risks to downstream communities from flooding and disruptions to power supplies across Central Asia if dams are damaged.

Earthquake shaking could impact flood risk within the Pamir by destabilizing existing natural dams, such as the Usoi landslide dam, built by a 2 km³ landslide mobilized by shaking from the 1911 M_w 7.3 Sarez Earthquake (Emmer et al., 2020; Hanisch, 2002; Kulikova et al., 2016). At a smaller scale, hundreds of glacial lakes have been identified across the Pamir, many of which are growing as glaciers retreat (Mergili et al., 2013). These represent both a source of water, and a hazard if the dams holding them fail. In 2002 the village of Dasht in the southern Pamir was inundated in such an event, killing tens of people and destroying many houses (Mergili & Schneider, 2011). Large earthquakes in the Vakhsh Valley may, therefore, pose risks outside the immediate epicentral region.

5.5. Do Observations of Small Earthquakes Elucidate Sources of Large Earthquakes?

A common method of understanding the seismo-tectonics of a region is to deploy a dense network of seismometers for periods ranging from months to years, and use the small, very frequent earthquakes of M < ~4 to find active faults, and to understand whether visible geological faults are active and whether they have the potential to produce large earthquakes (Duverger et al., 2018; Frepoli et al., 2011; Kufner et al., 2018; Schurr et al., 2014). This can be very valuable for highlighting the subterranean geometry of the faults (e.g., Kufner et al., 2018), as well as observing crustal thicknesses (Schneider et al., 2019), and may illuminate areas of locking or creeping on certain faults, essential for understanding their mechanics and hazard (e.g., Lin & Lapusta, 2018). Finally, it makes calibrated earthquake relocation studies, like this one, possible.

In our study the earthquakes >M6 highlight a trend that is not evident from micro-seismicity, namely the WNW alignment identified in Figure 10a-4 which we hypothesized in Section 5.1 constituted the greater part of the 1949 earthquake rupture. This fault is not highlighted by microseismicity in the same way as the Vakhsh Fault (Figure 10a-1), possibly because the 1949 released all stress on this fault and it is now locked and accumulating strain.

This has implications for hazard, because 1949 earthquake is part of a wider pattern of deadly continental earthquakes which have occurred on “cryptic” faults—faults which remain unknown until a major earthquake

happens on them within instrumental records. This risk has been highlighted for oceanic convergent margins above megathrusts (Jara-Muñoz et al., 2022), but is present within convergent continental settings as well.

One example is the 2020 M_w 6.4 Koryak Earthquake, in eastern Siberia (Salomon et al., 2025). This earthquake bears many similarities to the 1949 Khait Earthquake. Firstly, it nucleated on a previously unknown fault, which was not well expressed in the surface geomorphology prior to the earthquake. Secondly, it occurred in a convergent continental setting of the Pacific Cordillera in high mountains, far from the plate boundary. Thirdly, the causative fault has a strike inclined $\sim 45^\circ$ to the nearby geological suture, which we might expect to be the line of weakness likely to break in an earthquake.

A further example is the 2017 earthquake doublet that occurred near the Eastern Denali Fault (EDF) in Southern Alaska (Choi et al., 2021). These M_w 6.2 and M_w 6.3 earthquakes both ruptured more than 10 km from the EDF, with fault plane strikes at $\sim 30^\circ$ – 45° inclination to the EDF. Choi et al. (2021) suggest the EDF is now a geological suture, with the active deformation now occurring over a ~ 50 km wide zone further south. The Vakhsh Fault appears to be presently only taking up around half the deformation between the Pamir and Tian Shan, so it may be on its way to becoming a geological suture, with all strain distributed across the Pamir and Tian Shan.

6. Conclusions

We combine seismology and geomorphic analysis to shed light on the tectonic circumstances of the 1949 M_w 7.6 Khait Earthquake and how it relates to the large Vakhsh Fault. Using historical seismograms, we determined a focal mechanism with strike, dip and rake of 50 ± 20 , 80 ± 10 , and -20 ± 10 respectively. We used multiple event relocation algorithm MLOC to perform a relative relocation of 133 earthquakes of $M_w > 4$, including the 1949 earthquake. We used regional seismometer deployments from the 2000s to “calibrate” these locations and remove biases introduced by an assumed global seismic velocity model, resulting in locations with ~ 5 km formal uncertainty. We located the 1949 earthquake epicenter at (70.870° E, 39.336° N) at a depth of 22–24 km—significantly refining previous estimates of the 1949 earthquake location.

By analysing high resolution Worldview-3, Pleiades, and Open-Source imagery we mapped ~ 35 km of earthquake surface rupture. We found evidence for faulting in the Yasman Valley, north of the Vakhsh River, and discovered right-lateral strike slip offsets of 5–9 m. In addition, we found smaller dip slip offsets of ~ 1 –2 m. From alignments of 1949 earthquake aftershocks, we suggested that a further 50 km fault rupture occurred between the 1949 epicenter and the confluence of the Muksu and Kyzyl-Suu Rivers. In addition we estimate the slip rate of the Vakhsh Fault to be ~ 5.5 mm/yr since 18 kyr, about half the geodetic convergence rate between the Pamir and Tian Shan.

We conclude that the 1949 earthquake probably did not occur on the Vakhsh Fault, instead rupturing a previously unknown fault within the Tian Shan basement. The 1949 Earthquake demonstrates a change in tectonic regime caused by the recent closure of the intramontane Vakhsh basin. Compared to the simple overthrusting of the Alai Valley further east, in the Vakhsh Valley shortening is accommodated by a mixture of slip on the Vakhsh Fault, extrusion of the Peter I Range, and vertical axis rotations in the Tian Shan. The 1949 earthquake demonstrates the hazards posed by “cryptic” faults, and shows how studying early-instrumental earthquakes may elucidate them.

Appendix A: Arrivals Times and m_B Estimates From Digitized Waveforms of 1949 Khait Earthquake

The list of stations along with their respective arrival times for all phases recorded during the 1949 Khait earthquake, derived from the digitized waveforms. This table additionally presents the distances and azimuths to each station, as well as the amplitude and period values where applicable. In cases where the amplitude and period columns are left blank, it indicates that the actual amplitude cannot be determined.

Station name	Distance [$^{\circ}$]	Azimuth [$^{\circ}$]	Comp	Phase	Arrival time	T [sec]	Amp [μm]	m_B
ABU	50,812	73,406	Z	P	04:02:43,00	9	56	7.5
ABU	50,812	73,406	Z	PP	04:04:22,00	12	59	7.4
ABU	50,812	73,406	N	S	04:10:04,00	16	98	7.4
BER	45,283	320,178	Z	P	04:01:56,00	3	22	7.6
BER	45,283	320,178	Z	PP	04:03:19,00	3	38	7.8
BER	45,283	320,178	E	S	04:08:36,00	9	107	7.6
BER	45,283	320,178	E	SS	04:08:39,00	—	—	—
COL	72,026	16,328	Z	P	04:04:58,00	9	37	7.5
COL	72,026	16,328	Z	PP	04:07:39,00	12	41	7.6
COL	72,026	16,328	N	S	04:14:21,00	15	65	7.6
DBN	46,333	308,839	Z	P	04:02:02,00	3	17	7.6
DBN	46,333	308,839	Z	PP	04:03:50,00	5	21	7.3
DBN	46,333	308,839	E	S	04:08:54,00	5	31	7.4
DBN	46,333	308,839	E	SS	04:12:44,00	—	—	—
GTT	43,444	307,416	Z	P	04:01:32,00	4	45	7.6
GTT	43,444	307,416	Z	PP	04:03:16,00	7	65	7.6
GTT	43,444	307,416	E	S	04:03:16,00	9	87	7.5
HUA	139,672	302,663	Z	Pdiff	04:13:04,00	9	21	7.4
HUA	139,672	302,663	E	PP	04:16:04,00	10	27	7.4
HUA	139,672	302,663	E	SS	04:20:32,00	12	54	8.0
PAD	43,613	298,125	Z	P	04:01:35,00	3	25	7.4
PAD	43,613	298,125	Z	PP	04:03:26,00	6	39	7.4
PAD	43,613	298,125	E	S	04:03:26,00	6	167	7.9
PAS	106,708	7,851	Z	P	04:07:58,00	5	4	7.7
PAS	106,708	7,851	Z	PP	04:12:09,00	5	19	8.0
PAS	106,708	7,851	N	S	04:18:28,00	5	44	8.2
PAV	45,059	298,394	Z	P	04:03:01,00	4	23	7.7
PAV	45,059	298,394	E	S	04:13:17,00	9	51	7.5
PRT	44,081	296,083	Z	P	04:01:46,00	3	32	7.9
PRT	44,081	296,083	E	S	04:08:15,00	6	87	7.9
ROM	44,052	292,756	Z	P	04:01:41,00	5	59	7.6
ROM	44,052	292,756	Z	PP	04:03:05,00	5	32	7.5
ROM	44,052	292,756	E	S	04:08:19,00	12	253	7.9
TAR	47,822	292,799	Z	P	04:01:18,00	2	13	7.7
TAR	47,822	292,799	Z	PP	04:02:55,00	3	12	7.4
TAR	47,822	292,799	E	S	04:07:24,00	4	26	7.5
								Average m_B 7.6 ± 0.2
								Median m_B 7.6 ± 0.6

Appendix B: 1949 Surface Wave Magnitude Estimates

The amplitudes (Amp) and periods (T) of the surface waves generated by the 1949 Khait earthquake. The surface wave magnitude, indicated in the third column, is computed using the Prague-Moscow formula (Karnik et al., 1962) for each station, and the average magnitude M_s is provided along with one standard deviation.

Station (Instrument)	Period [sec]	Amplitude [μm]	Ms
ABU	22	1083	7.8
BER	16	623	7.6
COL	25	588	7.8
DBN	16	282	7.3
GTT	18	1223	7.9
HUA	27	86	7.4
PAD	13	617	7.7
PAS	25	145	7.4
PAV	15	600	7.6
ROM	19	647	7.6
Median			7.6
Average			7.6

Appendix C: 1949 Scalar Moment and Moment Magnitude (M_w) Estimates

Station	Lat	Lon	Mo/Nm	M_w
ABU	34,8603	135,5739	4,23E + 20	7.7
BER	60,3958	5,3050	2,00E + 20	7.5
COL	64,9000	-147,7933	5,20E + 20	7.7
DBN	52,1000	5,1800	5,72E + 20	7.8
GTT	51,5500	9,9667	1,76E + 20	7.4
HUA	-12,0384	-75,3228	1,05E + 21	7.9
PAD	45,4086	11,8878	5,68E + 20	7.8
PAS	34,1485	-118,1711	2,01E + 20	7.5
PAV	45,1833	9,1736	5,16E + 20	7.7
PRT	43,8800	11,0942	1,96E + 20	7.5
ROM	41,9033	12,5133	2,14E + 20	7.5
TAR	40,4750	17,2910	4,32E + 20	7.7
Average				7.6 ± 0.2
Median				7.7 ± 0.2

Appendix D: Instrument Constants for the Analog Instruments Whose Records Were Digitized and Used in This Study

The majority of analog seismic were defined by specific values of instrument constants: free period, damping, and an additional parameter for the magnification of the recording system. These parameters are presented in the Table and were derived from Charlier and Tison (1953) and McComb and West (1931), or from handwritten station books when available.

Nr	Station	Component	Instrument	Magnification (V)	Period (T_0 [sec])	Damping (h)
1	ABU (Abuyama, Japan)	Z	Wiechert	180	4	0.46
		EW	Wiechert	200	12	0.46

Appendix D
Continued

Nr	Station	Component	Instrument	Magnication (V)	Period (T_0 [sec])	Damping (h)
2	BER (Bergen, Norway)	NS	Wiechert	200	12	0.46
		Z	Wiechert	330	4.3	0.24
		EW	Wiechert	275	9.0	0.11
		NS	Wiechert	175	9.2	0.27
3	COL (College, USA)	Z	Sprengnether	4,000	2	
		EW	Sprengnether	4,000	16	
		NS	Sprengnether	4,000	16	
4	DBN (De Bilt, Netherlands)	Z	Galitzin	740	12	
		EW	Galitzin	310	25	
		NS	Galitzin	310	25	
5	GTT (Gottingen, Germany)	Z	Wiechert	233	3.6	0.26
		EW	Wiechert	145	10.5	0.43
		NS	Wiechert	154	9	0.29
6	HUA (Huancayo, Peru)	Z	Benioff	1,550	0.5	
		EW	Wenner	1,550	9	0.63
		NS	Wenner	1,550	8	0.68
7	PAD (Padova, Italy)	Z	Vicentini	100	6.2	0.22
		EW	Vicentini	100	6.2	0.22
		NS	Vicentini	100	6.2	0.22
8	PAS (Pasadena, USA)	Z	Benioff	2,000	90	0.8
		EW	Benioff	2,000	90	0.8
		NS	Benioff	2,000	90	0.8
9	PAV (Pavia, Italy)	Z	Wiechert	124.6	3.4	0.27
		EW	Wiechert	140.4	3.3	0.31
		NS	Wiechert	111.2	3.5	0.32
10	PRT (Rocca di Papa, Italy)	Z	Agamennone	100	6	
		EW	Agamennone	100	8	
		NS	Agamennone	100	8	
11	ROM (Rome, Italy)	Z	Galitzin	800	10.00	
		EW	Galitzin	800	9.80	
		NS	Galitzin	800	10.20	
12	TAR (Tarente, Italy)	Z	Vicentini	120	0.8	
		EW	Vicentini	100	2.40	
		NS	Vicentini	100	2.40	

Appendix E: Modified AK135 Crustal Velocity Model Used in *mloc* Inversion

Depth/km	Vp/km/s	Vs/km/s
0.000	5.800	3.150
5.000	5.800	3.150
5.000	5.900	3.500
20.000	5.900	3.500
20.000	6.300	3.750

Appendix E
Continued

Depth/km	Vp/km/s	Vs/km/s
50.000	6.300	3.750MOHO
50.000	8.100	4.550
77.500	8.100	4.550
120.000	8.100	4.550
165.000	8.175	4.550
210.000	8.300	4.550
210.000	8.300	4.553
260.000	8.483	4.609
310.000	8.665	4.696

Conflict of Interest

The authors declare no conflicts of interest relevant to this study.

Data Availability Statement

Code for the Ames Stereo Pipeline routine can be found at (Johnson, 2024) <https://doi.org/10.5281/zenodo.14453174>. Resulting point clouds can be found at Open Topography (Johnson, 2025) <https://doi.org/10.5069/G9GH9G5W>. Line mapping, *mloc* data, and historical seismogram data are available at (Johnson et al., 2024) <https://doi.org/10.5281/zenodo.14453364>. The *mloc* earthquake relocation software can be downloaded for free at <https://seismo.com/mloc/>. Arrival times for *mloc* were downloaded from <https://www.isc.ac.uk/>. Arrival times for events in the TIPAGE catalog were obtained from Bernd Schurr at GFZ Potsdam.

References

Acknowledgments
This work was supported by the Leverhulme Trust Research Project Grants "EROICA" (RPG-2018-371), NATO Science for Peace and Security Multi-Year Project G5690, the NERC-funded COMET (GA/13/M/031). Benedict Johnson is supported by the Oxford NERC-DTP (NE/S007474/1). Pleiades satellite imagery was obtained through the Committee for Earth Observing satellites Seismic Hazard demonstrator. We thank St. Edmund Hall, Oxford, for purchase of the Worldview-3 imagery. Maps were prepared using Generic Mapping Tools (GMT) software and PyGMT wrapper (Tian et al., 2024; Wessel et al., 2019) and used the Scientific Color Maps (Cramer, 2023). Phase arrival data from the TIPAGE and TIPTIMON seismic networks was provided by Bernd Schurr and Wasja Bloch. The text ends with an acknowledgment section and statement that includes:

- Any real or perceived financial conflicts of interests for any author.
- Other affiliations for any author that may be perceived as having a conflict of interest with respect to the results of this paper.
- Funding information related to the work for all authors should be entered in the form in GEMS as part of your submission. This form in GEMS uses the official Fundref list, which provides a link after publication that is available to funders. Any other funding information not listed in the GEMS form should be included in the acknowledgments and/or cover letter. It is also the appropriate place to thank colleagues and other contributors. AGU does not normally allow dedications.

- Abramowski, U., Bergau, A., Seebach, D., Zech, R., Glaser, B., Sosin, P., et al. (2006). Pleistocene glaciations of Central Asia: Results from ^{10}Be surface exposure ages of erratic boulders from the Pamir (Tajikistan), and the Alay–Turkestan range (Kyrgyzstan). *Quaternary Science Reviews*, 25(9–10), 1080–1096. <https://doi.org/10.1016/j.quascirev.2005.10.003>
- Aki, K., & Richards, P. G. (2002). Quantitative seismology (2nd ed.). Quant. Seismol.
- Altamimi, Z., Métivier, L., Rebischung, P., Rouby, H., & Collilieux, X. (2017). ITRF2014 plate motion model. *Geophysical Journal International*, 209, 1906–1912. <https://doi.org/10.1093/gji/ggx136>
- Ansal, A. (2015). In *Perspectives on European earthquake engineering and seismology: Volume 2, geotechnical, geological and earthquake engineering*. Springer International Publishing. Cham. <https://doi.org/10.1007/978-3-319-16964-4>
- Arrowsmith, J. R., & Strecker, M. R. (1999). Seismotectonic range-front segmentation and mountain-belt growth in the Pamir-Alai region, Kyrgyzstan (India-Eurasia collision zone). *Geological Society of America Bulletin*, 111(11), 1665–1683. [https://doi.org/10.1130/0016-7606\(1999\)111<1665:SRFSAM>2.3.CO;2](https://doi.org/10.1130/0016-7606(1999)111<1665:SRFSAM>2.3.CO;2)
- Benn, D. I., & Owen, L. A. (1998). The role of the Indian summer monsoon and the mid-latitude westerlies in Himalayan glaciation: Review and speculative discussion. *Journal of the Geological Society*, 155(2), 353–363. <https://doi.org/10.1144/gsjgs.155.2.0353>
- Berezyuk, N. (n.d.). OneGeology VSEGEI maps.
- Bergman, E. A., Benz, H. M., Yeck, W. L., Karasözen, E., Engdahl, E. R., Ghods, A., et al. (2023). A global catalog of calibrated earthquake locations. *Seismological Research Letters*, 94(1), 485–495. <https://doi.org/10.1785/0220220217>
- Beyer, R., Alexandrov, O., ScottMcMichael, Broxton, M., Lundy, M., Husmann, K., et al. (2021). NeoGeographyToolkit/StereoPipeline 3.0.0. <https://doi.org/10.5281/ZENODO.5140581>
- Beyer, R. A., Alexandrov, O., & McMichael, S. (2018). The Ames Stereo Pipeline: NASA's open source software for deriving and processing terrain data. *Earth and Space Science*, 5(9), 537–548. <https://doi.org/10.1029/2018EA000409>
- Bormann, P., & Saul, J. (2009). Earthquake magnitude. In *Encyclopedia of complexity and systems science* (pp. 2473–2496). Springer. New York, NY. https://doi.org/10.1007/978-0-387-30440-3_151
- Bormann, P., Wendt, S., & Klinge, K. (2013). Data analysis and seismogram interpretation (draft, under review). In *New Manual of Seismological Observatory Practice 2 (NMSOP-2); 14 mb* (p. 152). https://doi.org/10.2312/GFZ.NMSOP-2_CH11
- Bouchon, M., Bouin, M.-P., Karabulut, H., Toksöz, M. N., Dietrich, M., & Rosakis, A. J. (2001). How fast is rupture during an earthquake? New insights from the 1999 Turkey earthquakes. *Geophysical Research Letters*, 28(14), 2723–2726. <https://doi.org/10.1029/2001GL013112>
- Burtman, M. (1993). Geological and geophysical evidence for deep subduction of continental crust beneath the Pamir.
- Cadek, O. (1987). Studying earthquake ground motion in Prague from Wiechert seismograph records. In *Studying earthquake ground motion in Prague from Wiechert seismograph records* (Vol. 96, pp. 438–447).
- Campbell, G. E., Walker, R. T., Abdurakhmatov, K., Schwenninger, J., Jackson, J., Elliott, J. R., & Copley, A. (2013). The Dzungarian fault: Late Quaternary tectonics and slip rate of a major right-lateral strike-slip fault in the northern Tien Shan region. *Journal of Geophysical Research: Solid Earth*, 118(10), 5681–5698. <https://doi.org/10.1002/jgrb.50367>

- Charlier, C., & Tison, L. (1953). Comité National belge de Géodésie et de Géophysique. Rapport annuel. Année 1952. *Bulletin Géodesique*, 29(1), 295–297. <https://doi.org/10.1007/BF02525771>
- Chen, W.-P., & Molnar, P. (1977). Seismic moments of major earthquakes and the average rate of slip in central Asia. *Journal of Geophysical Research*, 82(20), 2945–2969. <https://doi.org/10.1029/JB082i020p02945>
- Choi, M., Eaton, D. W., & Enkelmann, E. (2021). Is the Eastern Denali fault still active? *Geology*, 49(6), 662–666. <https://doi.org/10.1130/G48461.1>
- Coutand, I., Strecker, M. R., Arrowsmith, J. R., Hilley, G., Thiede, R. C., Korjenkov, A., & Omuraliev, M. (2002). Late Cenozoic tectonic development of the intramontane Alai Valley, (Pamir-Tien Shan region, central Asia): An example of intracontinental deformation due to the Indo-Eurasia collision. *Tectonics*, 21(6), 3–1–3–19. <https://doi.org/10.1029/2002TC001358>
- Crameri, F. (2023). Scientific colour maps. <https://doi.org/10.5281/zenodo.8409685>
- Croux, C., & Rousseeuw, P. J. (1992). Time-efficient algorithms for two highly robust estimators of scale. In Y. Dodge & J. Whittaker (Eds.), *Computational statistics* (pp. 411–428). Physica-Verlag HD. Heidelberg. https://doi.org/10.1007/978-3-662-26811-7_58
- Dahm, T., & Krüger, F. (1999). Higher-degree moment tensor inversion using far-field broad-band recordings: Theory and evaluation of the method with application to the 1994 Bolivia deep earthquake. *Geophysical Journal International*, 137(1), 35–50. <https://doi.org/10.1046/j.1365-246x.1999.00761.x>
- Dahm, T., & Krüger, F. (2014). Moment tensor inversion and moment tensor interpretation. In *New Man. Seismol. Obs. Pract. 2 NMSOP2 3 mb* (p. 32). https://doi.org/10.2312/GFZ.NMSOP-2_IS_3.9
- Dortch, J. M., Owen, L. A., & Caffee, M. W. (2013). Timing and climatic drivers for glaciation across semi-arid western Himalayan–Tibetan orogen. *Quaternary Science Reviews*, 78, 188–208. <https://doi.org/10.1016/j.quascirev.2013.07.025>
- Duverger, C., Lambotte, S., Bernard, P., Lyon-Caen, H., Deschamps, A., & Nercessian, A. (2018). Dynamics of microseismicity and its relationship with the active structures in the western Corinth Rift (Greece). *Geophysical Journal International*, 215(1), 196–221. <https://doi.org/10.1093/gji/ggy264>
- Dziewonski, A. M., Chou, T.-A., & Woodhouse, J. H. (1981). Determination of earthquake source parameters from waveform data for studies of global and regional seismicity. *Journal of Geophysical Research*, 86(B4), 2825–2852. <https://doi.org/10.1029/JB086iB04p02825>
- Ekström, G., Nettles, M., & Dziewoński, A. M. (2012). The global CMT project 2004–2010: Centroid-moment tensors for 13,017 earthquakes. *Physics of the Earth and Planetary Interiors*, 200–201, 1–9. <https://doi.org/10.1016/j.pepi.2012.04.002>
- Elliott, A., Elliott, J., Hollingsworth, J., Kulikova, G., Parsons, B., & Walker, R. (2020). Satellite imaging of the 2015 M7.2 earthquake in the Central Pamir, Tajikistan, elucidates a sequence of shallow strike-slip ruptures of the Sarez-Karakul fault. *Geophysical Journal International*, 221(3), 1696–1718. <https://doi.org/10.1093/gji/ggaa090>
- Emmer, A., Harrison, S., Mergili, M., Allen, S., Frey, H., & Huggel, C. (2020). 70 years of lake evolution and glacial lake outburst floods in the Cordillera Blanca (Peru) and implications for the future. *Geomorphology*, 365, 107178. <https://doi.org/10.1016/j.geomorph.2020.107178>
- Engdahl, E. R., Giacomo, D. D., Sakarya, B., Gkaraouni, C. G., Harris, J., & Storchak, D. A. (2020). ISC-EHB 1964–2016, an improved data set for studies of Earth structure and global seismicity. *Earth and Space Science*, 7(1), e2019EA000897. <https://doi.org/10.1029/2019EA000897>
- Engdahl, E. R., van der Hilst, R., & Buland, R. (1998). Global teleseismic earthquake relocation with improved travel times and procedures for depth determination. *Bulletin of the Seismological Society of America*, 88(3), 722–743. <https://doi.org/10.1785/bssa0880030722>
- Evans, S. G., Roberts, N. J., Ischuk, A., Delaney, K. B., Morozova, G. S., & Tutubalina, O. (2009). Landslides triggered by the 1949 Khait earthquake, Tajikistan, and associated loss of life. *Engineering Geology*, 109(3–4), 195–212. <https://doi.org/10.1016/j.enggeo.2009.08.007>
- Frepoli, A., Maggi, C., Cimini, G. B., Marchetti, A., & Chiappini, M. (2011). Seismotectonic of Southern Apennines from recent passive seismic experiments. *J. Geodyn., Active Tectonics of the Circum-Adriatic Region*, 51(2–3), 110–124. <https://doi.org/10.1016/j.jog.2010.02.007>
- Gagala, L., Ratschbacher, L., Ringenbach, J.-C., Kufner, S.-K., Schurr, B., Dedow, R., et al. (2020). Tajik Basin and Southwestern Tian Shan, Northwestern India-Asia Collision Zone: 1. Structure, kinematics, and salt tectonics in the Tajik fold-and-thrust belt of the Western Foreland of the Pamir. *Tectonics*, 39(5), e2019TC005871. <https://doi.org/10.1029/2019TC005871>
- Grabovec, D., & Allegretti, I. (1994). On the digitizing of historical seismograms. *Geofizika*, 11, 27–31.
- Grin, E., Ehlers, T. A., Schaller, M., Sulaymonova, V., Ratschbacher, L., & Gloaguen, R. (2016). ^{10}Be surface-exposure age dating of the Last Glacial Maximum in the northern Pamir (Tajikistan). *Quaternary Geochronology*, 34, 47–57. <https://doi.org/10.1016/j.quageo.2016.03.007>
- Gubin, I. E. (1960). *Zakonomernost Seismicheskikh Proyavlenii na Territorii Tadzhikis-tana* (pp. 279–294). Akad. Nauk SSR Mosc.
- Hamburger, M. W., Swanson, W. A., & Popandopulo, G. A. (1993). Velocity structure and seismicity of the Garm region, Central Asia. *Geophys. Journal of Intelligence*, 115(2), 497–511. <https://doi.org/10.1111/j.1365-246X.1993.tb01202.x>
- Hanisch, J. (2002). Usoi landslide dam in Tajikistan—The world's highest dam. First stability assessment of the rock slopes at Lake Sarez. In *Landslides*. Routledge.
- Heimann, S., Kriegerowski, M., Isken, M., Cesca, S., Daout, S., Grigoli, F., et al. (2017). Pyrocko—An open-source seismology toolbox and library. <https://doi.org/10.5880/GFZ.2.1.2017.001>
- Heimann, S., Vasyura-Bathke, H., Sudhaus, H., Isken, M. P., Kriegerowski, M., Steinberg, A., & Dahm, T. (2019). A Python framework for efficient use of pre-computed Green's functions in seismological and other physical forward and inverse source problems. *Solid Earth*, 10(6), 1921–1935. <https://doi.org/10.5194/se-10-1921-2019>
- Hollingsworth, J., Jackson, J., Walker, R., Reza Gheitanchi, M., & Javad Bolourchi, M. (2006). Strike-slip faulting, rotation, and along-strike elongation in the Kopeh Dagh Mountains, NE Iran. *Geophysical Journal International*, 166(3), 1161–1177. <https://doi.org/10.1111/j.1365-246X.2006.02983.x>
- IEA. (2022). Tajikistan 2022 energy sector review.
- Ischuk, A., Bendick, R., Rybin, A., Molnar, P., Khan, S. F., Kuzikov, S., et al. (2013). Kinematics of the Pamir and Hindu Kush regions from GPS geodesy. *Journal of Geophysical Research: Solid Earth*, 118(5), 2408–2416. <https://doi.org/10.1002/jgrb.50185>
- Jackson, J., Molnar, P., Patton, H., & Fitch, T. (1979). Seismotectonic aspects of the Markansu Valley, Tadzhikstan, earthquake of August 11, 1974. *Journal of Geophysical Research*, 84(B11), 6157–6167. <https://doi.org/10.1029/JB084iB11p06157>
- Jara-Muñoz, J., Melnick, D., Li, S., Socquet, A., Cortés-Aranda, J., Brill, D., & Strecker, M. R. (2022). The cryptic seismic potential of the Pichilemu blind fault in Chile revealed by off-fault geomorphology. *Nature Communications*, 13(1), 3371. <https://doi.org/10.1038/s41467-022-30754-1>
- Johnson, B., Kulikova, G., Bergman, E., Kruger, F., Pierce, I., Hollingsworth, J., & Walker, R. (2024). Data from: “Rupture of the 1949 Khait earthquake on a cryptic fault: Implications for earthquake hazard.” [Dataset]. Zenodo. <https://doi.org/10.5281/ZENODO.14453365>
- Johnson, B. W. W. (2024). bwjohnson/asp_dem_creation: Ames stereo pipeline for worldview 3 template [Software]. Zenodo. <https://doi.org/10.5281/ZENODO.14453174>
- Johnson, B. W. W. (2025). Satellite stereo pointclouds of the Yasman and Vakhsh Valleys, Tajikistan [Dataset]. OpenTopography. <https://doi.org/10.5069/G9GH9G5W>

- Jordan, T. H., & Sverdrup, K. A. (1981). Teleseismic location techniques and their application to earthquake clusters in the South-Central Pacific. *Bulletin of the Seismological Society of America*, 71, 1105–1130.
- Karasözen, E., Nissen, E., Bergman, E. A., & Ghods, A. (2019). Seismotectonics of the Zagros (Iran) from Orogen-Wide, calibrated earthquake relocations. *Journal of Geophysical Research: Solid Earth*, 124(8), 9109–9129. <https://doi.org/10.1029/2019JB017336>
- Karasözen, E., Nissen, E., Bergman, E. A., Johnson, K. L., & Walters, R. J. (2016). Normal faulting in the Simav graben of western Turkey reassessed with calibrated earthquake relocations. *Journal of Geophysical Research: Solid Earth*, 121(6), 4553–4574. <https://doi.org/10.1002/2016JB012828>
- Karnik, V., Kondorskaya, N. V., Riznichenko, J. V., Savarensky, E. F., Soloviev, S. L., Shebalin, N. V., et al. (1962). Standardization of the earthquake magnitude scale. *Studia Geophysica et Geodetica*, 6(1), 41–48. <https://doi.org/10.1007/bf02590040>
- Kennett, B. L. N., Engdahl, E. R., & Buland, R. (1995). Constraints on seismic velocities in the Earth from traveltimes. *Geophysical Journal International*, 122(1), 108–124. <https://doi.org/10.1111/j.1365-246X.1995.tb03540.x>
- Kondorskaya, N., & Shebalin, N. (1982). New catalog of strong earthquakes in the U.S.S.R. from ancient times through 1977.
- Kufner, S.-K., Schurr, B., Ratschbacher, L., Murodkulov, S., Abdulhameed, S., Ischuk, A., et al. (2018). Seismotectonics of the Tajik Basin and surrounding Mountain ranges. *Tectonics*, 37(8), 2404–2424. <https://doi.org/10.1029/2017TC004812>
- Kufner, S.-K., Schurr, B., Sippl, C., Yuan, X., Ratschbacher, L., Akbar, A., et al. (2016). Deep India meets deep Asia: Lithospheric indentation, delamination and break-off under Pamir and Hindu Kush (Central Asia). *Earth and Planetary Science Letters*, 435, 171–184. <https://doi.org/10.1016/j.epsl.2015.11.046>
- Kulikova, G. (2016). Source parameters of the major historical earthquakes in the Tien-Shan region from the late 19th to the early 20th century.
- Kulikova, G., & Krüger, F. (2015). Source process of the 1911 M8.0 Chon-Kemin earthquake: Investigation results by analogue seismic records. *Geophysical Journal International*, 201, 1891–1911. <https://doi.org/10.1093/gji/ggv091>
- Kulikova, G., Schurr, B., Krüger, F., Brzoska, E., & Heimann, S. (2016). Source parameters of the Sarez-Pamir earthquake of 1911 February 18. *Geophysical Journal International*, 205(2), 1086–1098. <https://doi.org/10.1093/gji/ggw069>
- Leith, W., & Alvarez, W. (1985). Structure of the Vakhsh fold-and-thrust belt, Tadzhik SSR: Geologic mapping on a Landsat image base. *Geological Society of America Bulletin*, 96(7), 875–885. [https://doi.org/10.1130/0016-7606\(1985\)96<875:SOTVFB>2.0.CO;2](https://doi.org/10.1130/0016-7606(1985)96<875:SOTVFB>2.0.CO;2)
- Leonov, N. N. (1960). The Khait, 1949 earthquake and geological conditions of its occurrence. In *Izv. Acad. Sci. USSR Geophys. Ser.* (Vol. 3, pp. 409–424).
- Lin, Y.-Y., & Lapusta, N. (2018). Microseismicity simulated on asperity-like fault patches: On scaling of seismic moment with duration and seismological estimates of stress drops. *Geophysical Research Letters*, 45(16), 8145–8155. <https://doi.org/10.1029/2018GL078650>
- Lukk, A. A., Yunga, S. L., Shevchenko, V. I., & Hamburger, M. W. (1995). Earthquake focal mechanisms, deformation state, and seismotectonics of the Pamir-Tien Shan region, Central Asia. *Journal of Geophysical Research*, 100(B10), 20321–20343. <https://doi.org/10.1029/95JB02158>
- Mackenzie, D., & Elliott, A. (2017). Untangling tectonic slip from the potentially misleading effects of landform geometry. *Geosphere*, 13, 1310–1328. <https://doi.org/10.1130/GES01386.1>
- McCalpin, J. (2009). Paleoseismology. In *International geophysics series* (2nd ed.). Academic Press. Burlington, MA.
- McComb, H. E., & West, J. C. (1931). *List of seismologic stations of the world* (2nd ed.). The National Research Council of the National Academy of Sciences.
- Mechie, J., Schurr, B., Yuan, X., Schneider, F., Sippl, C., Minaev, V., et al. (2019). Observations of guided waves from the Pamir seismic zone provide additional evidence for the existence of subducted continental lower crust. *Tectonophysics*, 762, 1–16. <https://doi.org/10.1016/j.tecto.2019.04.007>
- Medvedev, S. W., Sponheuer, W., & Kárník, V. (1965). *Seismic intensity scale version MSK 1964*. International Association of Seismology and Physics of the Earth's Interior.
- Mergili, M., Müller, J. P., & Schneider, J. F. (2013). Spatio-temporal development of high-mountain lakes in the headwaters of the Amu Darya River (Central Asia). *Global and Planetary Change*, 107, 13–24. <https://doi.org/10.1016/j.gloplacha.2013.04.001>
- Mergili, M., & Schneider, J. F. (2011). Regional-scale analysis of lake outburst hazards in the southwestern Pamir, Tajikistan, based on remote sensing and GIS. *Natural Hazards and Earth System Sciences*, 11(5), 1447–1462. <https://doi.org/10.5194/nhess-11-1447-2011>
- Metzger, S., Gagala, Ł., Ratschbacher, L., Lazecký, M., Maghsoudi, Y., & Schurr, B. (2021). Tajik depression and Greater Pamir Neotectonics from InSAR rate maps. *Journal of Geophysical Research: Solid Earth*, 126(12), e2021JB022775. <https://doi.org/10.1029/2021JB022775>
- Metzger, S., Ischuk, A., Deng, Z., Ratschbacher, L., Perry, M., Kufner, S.-K., et al. (2020a). Dense GNSS profiles across the northwestern tip of the India-Asia collision zone: Triggered slip and westward flow of the Peter the First Range, Pamir, into the Tajik Depression. *Tectonics*, 39(2), e2019TC005797. <https://doi.org/10.1029/2019TC005797>
- Metzger, S., Ischuk, A., Deng, Z., Ratschbacher, L., Perry, M., Kufner, S.-K., et al. (2020b). Dense GPS profiles across the northwestern tip of the India-Asia collision zone: Triggered slip and westward flow of the Peter the First Range, Pamir, into the Tajik Depression. *Tectonics*, 39(2), e2019TC005797. <https://doi.org/10.1029/2019TC005797>
- Mikhailova, N. N., Mukambayev, A. S., Aristova, I. L., Kulikova, G., Ullah, S., Pilz, M., & Bindu, D. (2015). Central Asia earthquake catalogue from ancient time to 2009. *Annales Geophysicae*, 58(1), 2. <https://doi.org/10.4401/ag-6681>
- Hadjer, S., Ehlers, T. A., Bendick, R., Stübner, K., & Strube, T. (2016). A Quaternary fault database for central Asia. *Natural Hazards and Earth System Sciences*, 16(2), 529–542. <https://doi.org/10.5194/nhess-16-529-2016>
- Neil, E. A., & Houseman, G. A. (1997). Geodynamics of the Tarim Basin and the Tian Shan in central Asia. *Tectonics*, 16(4), 571–584. <https://doi.org/10.1029/97TC01413>
- Nissen, E., Tatar, M., Jackson, J. A., & Allen, M. B. (2011). New views on earthquake faulting in the Zagros fold-and-thrust belt of Iran. *Geophysical Journal International*, 186(3), 928–944. <https://doi.org/10.1111/j.1365-246X.2011.05119.x>
- Ou, Q., Kulikova, G., Yu, J., Elliott, A., Parsons, B., & Walker, R. (2020). Magnitude of the 1920 Haiyuan earthquake reestimated using seismological and geomorphological methods. *Journal of Geophysical Research: Solid Earth*, 125(8), e2019JB019244. <https://doi.org/10.1029/2019JB019244>
- Patyniak, M., Landgraf, A., Dzhumabaeva, A., Baikulov, S., Williams, A. M., Weiss, J. R., et al. (2021). The Pamir Frontal Thrust fault: Holocene full-segment ruptures and implications for complex segment interactions in a continental collision zone. *Journal of Geophysical Research: Solid Earth*, 126(12), e2021JB022405. <https://doi.org/10.1029/2021JB022405>
- Rautian, T. G., Khalturin, V. I., Fujita, K., Mackey, K. G., & Kendall, A. D. (2007). Origins and methodology of the Russian energy K-class system and its relationship to magnitude scales. *Seismological Research Letters*, 78(6), 579–590. <https://doi.org/10.1785/gssrl.78.6.579>
- Rizza, M., Abdurakhmatov, K., Walker, R., Braucher, R., Guillou, V., Carr, A. S., et al. (2019). Rate of slip from multiple quaternary dating methods and paleoseismic investigations along the Talas-Fergana Fault: Tectonic implications for the Tien Shan Range. *Tectonics*, 38(7), 2477–2505. <https://doi.org/10.1029/2018TC005188>

- Röhringer, I., Zech, R., Abramowski, U., Sosin, P., Aldahan, A., Kubik, P. W., et al. (2012). The late Pleistocene glaciation in the Bogchirgir Valleys (Pamir, Tajikistan) based on ^{10}Be surface exposure dating. *Quaternary Research*, 78(3), 590–597. <https://doi.org/10.1016/j.yqres.2012.09.002>
- Sadovsky, M. A., & Nersesov, I. L. (1974). Forecasts of earthquakes on the basis of complex geophysical features. *Tectonophysics, Focal processes and the prediction of earthquakes*, 23(3), 247–255. [https://doi.org/10.1016/0040-1951\(74\)90024-9](https://doi.org/10.1016/0040-1951(74)90024-9)
- Saks, T., Rinterknecht, V., Lavrentiev, I., Béra, G., Mattea, E., & Hoelzle, M. (2024). Acceleration of Abramov Glacier (Pamir-Alay) retreat since the Little Ice Age. *Boreas*, 53(3), 415–429. <https://doi.org/10.1111/bor.12659>
- Salomon, G., Nissen, E., Tan, F., Bergman, E., Sloan, A., & Pousse-Beltran, L. (2025). The 2020 Mw 6.4 Koryak Highlands earthquake illustrates hidden seismic hazards in the northern Pacific Cordillera. *Geophysical Journal International*, 240(3), 2111–2124. <https://doi.org/10.1093/gji/ggaf031>
- Scherbaum, F. (2006). *Of poles and zeros: Fundamentals of digital seismology*. Springer Science & Business Media.
- Schneider, F. M., Yuan, X., Schurr, B., Mechic, J., Sippl, C., Haberland, C., et al. (2013). Seismic imaging of subducting continental lower crust beneath the Pamir. *Earth and Planetary Science Letters*, 375, 101–112. <https://doi.org/10.1016/j.epsl.2013.05.015>
- Schneider, F. M., Yuan, X., Schurr, B., Mechic, J., Sippl, C., Kufner, S.-K., et al. (2019). The crust in the Pamir: Insights from receiver functions. *Journal of Geophysical Research: Solid Earth*, 124(8), 9313–9331. <https://doi.org/10.1029/2019JB017765>
- Schultz, R. A. (2000). Localization of bedding plane slip and backthrust faults above blind thrust faults: Keys to wrinkle ridge structure. *Journal of Geophysical Research*, 105(E5), 12035–12052. <https://doi.org/10.1029/1999JE001212>
- Schurr, B., Ratschbacher, L., Sippl, C., Gloaguen, R., Yuan, X., & Mechic, J. (2014). Seismotectonics of the Pamir. *Tectonics*, 33(8), 1501–1518. <https://doi.org/10.1002/2014TC003576>
- Schwab, M., Ratschbacher, L., Siebel, W., McWilliams, M., Minaev, V., Lutkov, V., et al. (2004). Assembly of the Pamirs: Age and origin of magmatic belts from the southern Tien Shan to the southern Pamirs and their relation to Tibet. *Tectonics*, 23(4). <https://doi.org/10.1029/2003TC001583>
- Schweitzer, J. (2001). HYPOSAT—An enhanced routine to locate seismic events. *Pure and Applied Geophysics*, 158(1), 277–289. <https://doi.org/10.1007/PL000001160>
- Schweitzer, J. (2018). User manual for HYPOSAT 6 and HYPOMOD 2. New Man. In *Seismol. Obs. Pract. 2 NMSOP2 216 kB* (p. 38). https://doi.org/10.2312/GFZ.NMSOP_3_PD_111
- Seong, Y. B., Owen, L. A., Yi, C., & Finkel, R. C. (2009). Quaternary glaciation of Muztag Ata and Kongur Shan: Evidence for glacier response to rapid climate changes throughout the Late Glacial and Holocene in westernmost Tibet. *Geological Society of America Bulletin*, 121(3–4), 348–365. <https://doi.org/10.1130/B26339.1>
- Shean, D. E., Alexandrov, O., Moratto, Z. M., Smith, B. E., Joughin, I. R., Porter, C., & Morin, P. (2016). An automated, open-source pipeline for mass production of digital elevation models (DEMs) from very-high-resolution commercial stereo satellite imagery. *ISPRS Journal of Photogrammetry and Remote Sensing*, 116, 101–117. <https://doi.org/10.1016/j.isprsjprs.2016.03.012>
- Shearer, P. M. (2019). *Introduction to seismology*. Cambridge University Press.
- Sippl, C., Schurr, B., Tympel, J., Angiboust, S., Mechic, J., Yuan, X., et al. (2013). Deep burial of Asian continental crust beneath the Pamir imaged with local earthquake tomography. *Earth and Planetary Science Letters*, 384, 165–177. <https://doi.org/10.1016/j.epsl.2013.10.013>
- Sippl, C., Schurr, B., Yuan, X., Mechic, J., Schneider, F. M., Gadoev, M., et al. (2013). Geometry of the Pamir-Hindu Kush intermediate-depth earthquake zone from local seismic data. *Journal of Geophysical Research: Solid Earth*, 118(4), 1438–1457. <https://doi.org/10.1002/jgrb.50128>
- Sobel, E. R., Chen, J., Schoenbohm, L. M., Thiede, R., Stockli, D. F., Sudo, M., & Strecker, M. R. (2013). Oceanic-style subduction controls late Cenozoic deformation of the Northern Pamir orogen. *Earth and Planetary Science Letters*, 363, 204–218. <https://doi.org/10.1016/j.epsl.2012.12.009>
- Stanyukovich, K. (1997). *In the mountains of Pamir and Tien-Shan*. InMysl' Publishing House. Moscow.
- Storchak, D. A., Di Giacomo, D., Engdahl, E. R., Harris, J., Bondár, I., Lee, W. H. K., et al. (2015). The ISC-GEM global instrumental earthquake catalogue (1900–2009): Introduction. *Physics of the Earth and Planetary Interiors*, 239, 48–63. <https://doi.org/10.1016/j.pepi.2014.06.009>
- Storchak, D. A., Harris, J., Brown, L., Lieser, K., Shumba, B., & Di Giacomo, D. (2020). Rebuild of the bulletin of the international seismological centre (ISC)—Part 2: 1980–2010. *Geoscience Letters*, 7(1), 18. <https://doi.org/10.1186/s40562-020-00164-6>
- Storchak, D. A., Harris, J., Brown, L., Lieser, K., Shumba, B., Verney, R., et al. (2017). Rebuild of the bulletin of the international seismological centre (ISC), part 1: 1964–1979. *Geoscience Letters*, 4(1), 32. <https://doi.org/10.1186/s40562-017-0098-z>
- Strom, A., & Abdrakhmatov, K. (2018). *Rockslides and rock avalanches of Central Asia: Distribution, morphology, and internal structure*. Elsevier. Amsterdam, Netherlands; Cambridge, MA, United States.
- Stübner, K., Bookhagen, B., Merchel, S., Lachner, J., & Gadoev, M. (2021). Unravelling the Pleistocene glacial history of the Pamir Mountains, Central Asia. *Quaternary Science Reviews*, 257, 106857. <https://doi.org/10.1016/j.quascirev.2021.106857>
- Stübner, K., Grin, E., Hidy, A. J., Schaller, M., Gold, R. D., Ratschbacher, L., & Ehlers, T. (2017). Middle and Late Pleistocene glaciations in the southwestern Pamir and their effects on topography. *Earth and Planetary Science Letters*, 466, 181–194. <https://doi.org/10.1016/j.epsl.2017.03.012>
- Tadono, T., Ishida, H., Oda, F., Naito, S., Minakawa, K., & Iwamoto, H. (2014). Precise global DEM generation by ALOS PRISM. In *ISPRS Ann. Photogramm. Remote Sens. Spat. Inf. Sci. II-4* (pp. 71–76). <https://doi.org/10.5194/isprsaannals-II-4-71-2014>
- Takaku, J., Tadono, T., & Tsutsui, K. (2014). Generation of high resolution global DSM from ALOS PRISM. In *Int. Arch. Photogramm. Remote Sens. Spat. Inf. Sci. XL-4* (pp. 243–248). <https://doi.org/10.5194/isprsaarchives-XL-4-243-2014>
- Talebian, M., & Jackson, J. (2004). A reappraisal of earthquake focal mechanisms and active shortening in the Zagros mountains of Iran. *Geophysical Journal International*, 156(3), 506–526. <https://doi.org/10.1111/j.1365-246X.2004.02092.x>
- The GIMP Development Team. (2025). GNU image manipulation program (GIMP), version 3.0.6. Community, free software (license gplv3) [Computer software]. <https://gimp.org/>
- Tian, D., Uieda, L., Leong, W. J., Fröhlich, Y., Schlüter, W., Grund, M., et al. (2024). PyGMT: A Python interface for the generic mapping tools. <https://doi.org/10.5281/zenodo.13679420>
- Trifonov, V. G. (1978). Late Quaternary tectonic movements of western and central Asia. *Geological Society of America Bulletin*, 89(7), 1059–1072. [https://doi.org/10.1130/0016-7606\(1978\)89<1059:LQTMOW>2.0.CO;2](https://doi.org/10.1130/0016-7606(1978)89<1059:LQTMOW>2.0.CO;2)
- Tsai, C.-H., Abdrakhmatov, K., Mukambayev, A., Elliott, A. J., Elliott, J. R., Grützner, C., et al. (2022). Probing the upper end of intracontinental earthquake magnitude: A prehistoric example from the Dzhungarian and Lepsy faults of Kazakhstan. *Tectonics*, 41(10), e2022TC007300. <https://doi.org/10.1029/2022TC007300>
- Villaseñor, A., & Engdahl, E. R. (2005). A digital hypocenter catalog for the international seismological summary. *Seismological Research Letters*, 76(5), 554–559. <https://doi.org/10.1785/gssrl.76.5.554>

- Wang, J., Zhou, S., Zhao, J., Zheng, J., & Guo, X. (2011). Quaternary glacial geomorphology and glaciations of Kongur Mountain, eastern Pamir, China. *Science China Earth Sciences*, 54(4), 591–602. <https://doi.org/10.1007/s11430-010-4165-y>
- Wessel, P., Luis, J. F., Uieda, L., Scharroo, R., Wobbe, F., Smith, W. H. F., & Tian, D. (2019). The generic mapping tools version 6. *Geochemistry, Geophysics, Geosystems*, 20(11), 5556–5564. <https://doi.org/10.1029/2019GC008515>
- Weston, J., Engdahl, E. R., Harris, J., Di Giacomo, D., & Storchak, D. A. (2018). ISC-EHB: Reconstruction of a robust earthquake data set. *Geophysical Journal International*, 214(1), 474–484. <https://doi.org/10.1093/gji/ggy155>
- Wimpenny, S., & Watson, C. S. (2020). gWFM: A global catalog of moderate-magnitude earthquakes studied using teleseismic body waves. *Seismological Research Letters*, 92(1), 212–226. <https://doi.org/10.1785/0220200218>
- Wood, H. (1921). *A list of seismologic stations of the world*. Bulletin of the National Research Council.
- Yablokov, A. (2001). The tragedy of khait: A natural disaster in Tajikistan. *Mountain Research and Development*, 21(1), 91–93. [https://doi.org/10.1659/0276-4741\(2000\)021\[0091:TTOKAN\]2.0.CO;2](https://doi.org/10.1659/0276-4741(2000)021[0091:TTOKAN]2.0.CO;2)
- Zech, R., Abramowski, U., Glaser, B., Sosin, P., Kubik, P. W., & Zech, W. (2005). Late Quaternary glacial and climate history of the Pamir Mountains derived from cosmogenic ^{10}Be exposure ages. *Quaternary Research*, 64(2), 212–220. <https://doi.org/10.1016/j.yqres.2005.06.002>
- Zielke, O., & Arrowsmith, J. R. (2012). LaDiCaoz and LiDARimager—MATLAB GUIs for LiDAR data handling and lateral displacement measurement. *Geosphere*, 8, 206–221. <https://doi.org/10.1130/GES00686.1>
- Zubovich, A., Schöne, T., Metzger, S., Mosienko, O., Mukhamediev, S., Sharshbaev, A., & Zech, C. (2016). Tectonic interaction between the Pamir and Tien Shan observed by GPS. *Tectonics*, 35(2), 283–292. <https://doi.org/10.1002/2015TC004055>
- Zubovich, A. V., Wang, X., Scherba, Y. G., Schelochkov, G. G., Reilinger, R., Reigber, C., et al. (2010). GPS velocity field for the Tien Shan and surrounding regions. *Tectonics*, 29(6). <https://doi.org/10.1029/2010TC002772>